A Realistic Sub-grid Supernova Implementation for Exploring Supernova-Driven Turbulence

Jacob Mathew Buete

A thesis submitted in partial fulfillment of the degree of
Bachelor of Science (Advanced) (Honours) at
The Research School of Astronomy and Astrophysics
The Australian National University

October 2016

© Jacob Mathew Buete

Except where otherwise indicated, this thesis is my own original work.

Jacob Mathew Buete
27 October 2016

Acknowledgements

I would like to thank my supervisor, Dr Christoph Federrath, for all of his help and guidance throughout this project. I would also like to thank Matthew Alger for proof-reading this thesis a couple of times and listening to me lament that ‘everything is broken’ more times than I care to remember. Finally, I would like to thank my parents for their unending support throughout the years and many tired, stressed phone calls.

Abstract

Supernovae have a wide range of impacts on the development of the large scale structure in the galaxy. The shock from a supernova generates turbulence in the surrounding environment that can have significant effects of the evolution of the interstellar medium. Supernova-driven turbulence can disrupt the development of existing stellar nurseries and cause the creation of new stellar nurseries through the compression of nearby gas. This in turn has lasting effects on the local star formation rate, star formation efficiency, and the initial mass function — all areas where we are actively trying to understand the processes involved in their generation.

This makes supernovae indispensable for accurately simulating the evolution of the interstellar medium. However, many current supernova implementations make significant assumptions about the internal structure, size, or energy distribution of the supernova that are not in line with with the accepted literature. In this thesis I present a sub-grid model for examining supernova feedback using FLASH4. The model implements the Sedov solution to insert density, internal energy, and velocity profiles that are consistent with the current analytical models for the structure and propagation of supernova blast waves.

I found that the internal energy is a necessary component for the spherical evolution of the blast wave, and that the evolution of a naïve implementation in isothermal or polytropic gas — i.e. without the increased internal energy — is highly dependent on the initial size of the inserted supernova. An ideal equation of state works best for the simulations, provided a cooling function is also implemented as the temperatures introduced by a supernova can dominate the evolution of a simulation if left unchecked.

I applied the supernova implementation to examine supernova-driven turbulence within a 250 pc box, with resolutions of 128^3 and 256^3. I found that the generated turbulence was transonic, with a density distribution indicative of a two-phase medium resulting from the high supernova temperatures, and the lower bounds on cooling function used. I also found the density power spectrum to be consistent throughout the simulations, scaling as $k^{-1.67}$ in line accepted values for transonic weakly compressive turbulence for an isothermal gas. The velocity power spectrum varied significantly throughout the simulations due to discretised driving from the supernovae events; averaging over 35 Myr yielded a power law of $k^{-2.19}$ in line with the Burgers model of compressive turbulence.

Contents

Acknowledgements **v**

Abstract **vii**

1 Introduction **1**
- 1.1 Thesis Outline 2
- 1.2 Contributions 2

2 Background **3**
- 2.1 Supernovae 3
  - 2.1.1 Formation and Evolution of a Star 3
  - 2.1.2 Death of a Star 5
  - 2.1.3 The Structure of a Supernova 6
- 2.2 Supernova-Driven Turbulence 7
  - 2.2.1 What is Turbulence? 7
  - 2.2.2 Types of Turbulent Driving 8
  - 2.2.3 The Role of Turbulence in Large Scale Evolution 9
- 2.3 Numerical Methods for Hydrodynamic Simulations 10
  - 2.3.1 FLASH 10
  - 2.3.2 Hydrodynamic Solvers 10
  - 2.3.3 Types of Hydrodynamic Solvers 11
  - 2.3.4 Bouchut Solvers 11
  - 2.3.5 Convergence Conditions for Numerical Methods 12

3 The Sedov Solution **13**
- 3.1 Background 13
- 3.2 Derivation 14
  - 3.2.1 Assumptions of the Sedov Solution 14
    - 3.2.1.1 List of Physical Assumptions 14
  - 3.2.2 Initial Conditions 14
  - 3.2.3 Deriving the Self-Similarity Variable 16
  - 3.2.4 Creating Ansätze and Solving the Euler Equation 17
  - 3.2.5 Generating Radial Profiles 19
- 3.3 Defining the End of the Sedov Solution 21

4 Development of the Supernova Module 25
- 4.1 Design Philosophy 25
- 4.2 Dependence on Prior Work 25
  - 4.2.1 Sink Particles 26
- 4.3 Generating the Sedov Profiles 26
  - 4.3.1 Sampling Rates 27
- 4.4 Supernova Eligibility 28
  - 4.4.1 Mass Requirement 28
  - 4.4.2 Age Requirement 28
  - 4.4.3 The 'Supernova Time' 28
- 4.5 Interpolating into the Free Expansion Phase 29
    - 4.5.0.1 Implementation of the Free Expansion Phase 31
- 4.6 Conservation Methods 31
- 4.7 Tests of the Supernova Implementation 33
- 4.8 Using the Isothermal Equation of State 34
  - 4.8.1 Initial Testing 34
  - 4.8.2 Introducing a Smoothing Function 35
    - 4.8.2.1 The Mathematical Basis for Smoothing 36
    - 4.8.2.2 Implementation Details 38
    - 4.8.2.3 Examining the Results 39
  - 4.8.3 Radial Testing of the Supernova Implementation 40
- 4.9 Using the Polytropic Equation of State 40
  - 4.9.1 Testing for Radial Dependence 41
  - 4.9.2 Exploring the Effects of Resolution Levels 42
- 4.10 Using the Ideal Equation of State 43
  - 4.10.1 Testing for Dependence on Physical Size 44
  - 4.10.2 Approaching the Analytical Solution 46
    - 4.10.2.1 Extending the Sedov Solution to Include Internal Energy 46
    - 4.10.2.2 Determining the Energy Partition 47
  - 4.10.3 Modifying the Sedov Solution for Faster Simulations 49
- 4.11 Introducing Cooling to the Simulations 51

5 The Supernova-Driven Box 55
- 5.1 Motivation for the Supernova-Driven Box 55
- 5.2 Implementation of Random Supernovae 55
- 5.3 Simulation Parameters 56
- 5.4 Required Modifications to the Supernova Module 56
- 5.5 Projections of the Simulation 57
- 5.6 Analysis 58
  - 5.6.1 Examining the Distributions 59
  - 5.6.2 Examining the Power Spectra 62
- 5.7 Future Work 65

6 Conclusion 67

Bibliography **69**

Chapter 1

Introduction

In 1992 Matthew Choptuik submitted a paper in which he presented the first simulation of the collapse of a gravitational singularity [Choptuik 1993]. In this paper he presented evidence from his simulations to support a series of conjectures about scaling laws and the universality of the gravitational collapse of a black hole. These conjectures are now known as Choptuik scaling [Peleg et al. 1997]. This serves as classic example of numerical simulations informing the discovery of universal laws; simulation driven research.

A current problem facing astrophysicists is reconciling the discrepancy between the observed star formation rate, the star formation efficiency, and our understanding of the processes involved. Naïve models for the star formation rate greatly overestimate the rates and efficiencies compared with observed values. Recent efforts resolve this issue have focussed on the role of turbulence in the evolution of the interstellar medium [Mac Low and Klessen 2004; Elmegreen and Scalo 2004; Hennebelle and Falgarone 2012; Federrath and Klessen 2012; Padoan et al. 2014]. This turbulence can be generated by the movement of ionised gas, outflows generated during star formation [Federrath et al. 2014], or the heating produced by supernova explosions.

In order to test these theories we use simulations. They allow us to introduce a variety of changes to an identical set of initial conditions, and then determine the impact of each of the changes independently. This process has been widely used in the examination of the types and sources of turbulence needed to replicate our observations.

In this thesis I present an implementation of supernovae that can be used in the hydrodynamics code FLASH [Fryxell et al. 2000] to study the impact of supernova-driven turbulence on the evolution of large scale structure in gas clouds, as well as the star formation rate and efficiency within a given region. I avoid many of the assumptions made by previous supernova implementations, such as introducing uniform density and energy distributions, or inserting only thermal energy. Instead, I use the Sedov solution as a basis for my implementation.

The Sedov solution is an analytical representation of the structure of a blast wave [Sedov 1959], and is often used as a benchmark for supernova implementations to ensure that the implementation approaches the analytical Sedov solution over time. My model bypasses this step by implementing the Sedov solution itself, and can be shown to exactly match the theoretical evolutionary process for a supernova.

1.1 Thesis Outline

In Chapter 2 I present an overview of the knowledge that thesis assumes. I first provide a description of supernovae, where they come from, their relationship with stars and stellar formation, and the evolutionary process of the shockwave produced by the supernova. Following this I briefly covers the basics of turbulence, its relationship to the large-scale evolution of gas clouds, and the star formation rate and efficiency. Finally, I present a the reader with a crash course on numerical methods for hydrodynamic simulations and why they are important.

In Chapter 3 I derive the analytical Sedov solution, beginning with the underlying assumptions, providing a basis for the physics used, and deriving the self-similar nature of the solution. This chapter describes the method for generating the solution numerically, and calculating conditions under which the solution breaks down and is no longer deemed valid.

Chapter 4 represents the bulk of this thesis as I present the development process of the supernova module. I start with an overview of my design philosophy for the module, and some necessary information about the specifics of working within FLASH. I then present the results of the testing process, and discuss how the results informed the development of the module, and my own understanding of the Sedov solution.

In Chapter 5 I present an application of the supernova module to examine supernova-driven turbulence within a closed environment. I first discuss the motivation for the experiment, the set-up, and modifications that needed to be made to the module. I then present an analysis of the results, explaining the motivations for the different analytical techniques and comparing the results to past studies of turbulence.

1.2 Contributions

My main contribution in writing this thesis is the creation of the supernova module. This was implemented in FLASH4, and will be available for general use in future work if needed. It will be a permanent submodule of the Sink Particle module that can be enabled or disabled at the user's discretion.

To my knowledge this module is also the only supernova implementation to use the analytical Sedov solution. As such, this module also presents an opportunity to explore the differences between an implementation of the analytic solution, and models using far simpler assumptions.

There are currently plans to use the module for another set of simulations after the end of this project. This will consist of a large-scale simulation of the evolution of a molecular cloud, including models of all stages of stellar evolution, to examine the effect that supernova-driven turbulence has on the star formation rate, in addition to other forms of turbulent driving found in [Federrath et al. 2014].

Chapter 2

Background

In this chapter I present the background knowledge assumed by this thesis. I begin with an overview of what supernovae are, and their relationship to stars and stellar evolution. I also present the phases of supernova evolution before introducing the concept of supernova-driven turbulence, and providing a brief overview of what turbulence is and its effect on galactic structure. Finally I present the reader with a brief discussion on numerical methods used in simulations, what hydrodynamic solvers are, and what they are used for.

2.1 Supernovae

A *supernova* is in essence a big explosion, potentially the biggest kind of explosion that exists [Dong et al. 2016]. They occur at the end of the life cycle of *massive* stars, and represent some of the most energetic events that regularly occur throughout the galaxy. The brightness of a new supernova can outshine the light produced by entire galaxies, and can even be seen with the naked eye if the star is close enough to Earth [Green 2002].

Supernovae also produce significant amounts of energy, on the order of 10^{51} ergs. This energy is transferred into the surrounding medium through two mechanisms: radiation of thermal energy, and kinetic energy from the expanding shell. Both of these pathways mean that the majority of the energy from the supernova explosion is deposited back into its surroundings. The rate of expansion of the shell is also extremely fast — on the order of 10^4 km/s during the initial stages of expansion.

Due to the large amount of energy that is being injected into its surroundings, a supernova can have a significant impact on the evolution of the surrounding region: from affecting the local star formation, to large-scale effects on the distribution of gas within the local gas cloud [Mac Low et al. 2005], to driving the mechanism for galactic fountains [Bregman 1980].

2.1.1 Formation and Evolution of a Star

At its most basic level, a *star* is a sphere of plasma that is held together under its own gravity. At the centre of a star a thermonuclear process burns away, heating the core and generating vast amounts of energy that radiates away in the form of electromagnetic waves.

$$\frac{GM_{enc}m}{r} \approx \frac{1}{2}mv^2 \tag{2.1}$$

In the most general case the formation of a star is a result of the *gravitational collapse* of a gas cloud. By the *virial theorem*, see (2.1), a gas cloud is stable if the gravitational potential energy at a point r inside the cloud is equal to the kinetic energy at that point. If the gravitational potential energy is larger than the kinetic energy the cloud will begin to collapse.

$$\frac{dp}{dr} < -\frac{GM_{enc}\rho}{r^2} \tag{2.2}$$

An equivalent relationship is the Jeans instability [Jeans 1902], see (2.2), that relates the pressure inside a cloud to the enclosed mass and the density ρ at the point r. We most commonly use (2.2) to define a mass limit, referred to as the *Jeans mass*, that once achieved allows the region to enter a *gravitational free-fall*. The time scale for this process is described by (2.3):

$$t_{ff} \propto \sqrt{\frac{3\pi}{32G\rho}}. \tag{2.3}$$

We will note that the free-fall time is actually independent of the size of the region that is undergoing collapse, but rather only relies on the density within the region. During this process the density and pressure at the centre of the collapse is continually rising, until there is enough energy for the thermonuclear process to begin and a star to be born.

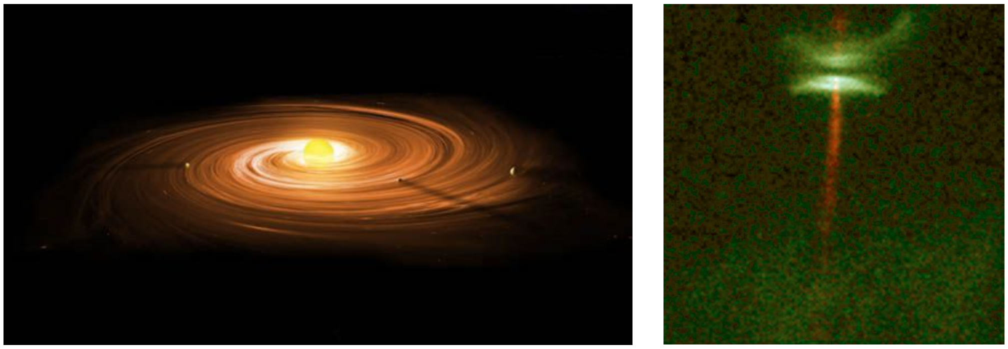

(a) (b)

Figure 2.1: (a) An artist's impression of an accretion disk surrounding a newly formed star *(Image: ANU ScienceWise)*. (b) An image of the accretion disk and magnetic jet outflows of HH-30 in Taurus *(Image: NASA. Hubble-Space Telescope, Optical)*.

Once the internal reaction has been started the star continues to accrete matter through *accretion discs*, though it starts to ablate the disk as it heats up [Getman et al. 2009]. It will also form two *jet outflows* to eject around some of the mass [Estalella 2013], generating some turbulence in the surrounding region [Federrath et al. 2014].

While we have focussed until this point on describing a single star undergoing formation, however due to the structure of gas clouds this process will typically occur many times in close proximity and in parallel. These regions are referred to as *stellar nurseries* and can be formed either through self-gravitation of a particularly dense region of a molecular gas cloud [Stahler and Palla 2008] or they can be the result of *triggered star formation* that I will discuss in §2.2.3.

At this point in the evolution of the star it reaches the main portion of its lifetime. The star will continue to burn through its hydrogen reserves and form heavy elements in the centre for anywhere from hundreds of millions of years to hundreds of billions of years. This wide range is due to a fundamental fact that the larger a star is, the brighter it is[Eddington 1924]. The brightness of a star is directly correlated with the amount of energy that it outputs, which is in turn a function of the rate at which the internal nuclear reaction is progressing. The faster a nuclear reaction is, the more material it will burn through. This leads to the key relationship for stellar lifetimes, big stars die young.

2.1.2 Death of a Star

The size of a given star has a significant impact on the the later stages of its lifetime. Stars with a mass of less than 8 $M_\odot$ eventually become a *white dwarf* [Weidemann and Koester 1983]. This evolution is triggered by the star running out of hydrogen to burn. For very low-mass stars the thermonuclear process will end here. Slightly larger stars will continue to burn helium for some period of time, slowing forming an carbon and oxygen core, and expelling its outer layers.

Any white dwarf with a core above the Chandrasekhar mass limit (1.44 $M_\odot$) is able to burn carbon. This is one of the fundamental requirements for the generation of a *Type Ia* supernova [Chandrasekhar 1935]. Type Ia can either occur from existing white dwarf progenitors that have a core mass above this limit, or from white dwarves accreting mass from neighouring stars in a binary system. Type Ia supernovae are characterised as a run-away nuclear process: as the core of the star begins fusing carbon it becomes more dense, the internal pressure rises, and the reaction rate increases thus entering into a feedback loop. The end result is a thermonuclear explosion that obliterates much of the star.

The other type of supernova occurs at the other end of the stellar mass scale, with stars above 8 $M_\odot$. These are referred to as *core-collapse* supernovae, and can be decomposed into three main types: Type Ib, Type Ic, and Type II. For the purposes of this thesis I will only discuss the latter as observations put the relative abundance of Type Ib/Ic at 12.7% of observed supernovae, compared to 59.7% and 27.6% for Type Ia and Type II respectively [Cappellaro et al. 1999; Mannucci et al. 2008].

Type II supernovae occur during the expansion phase of massive stars when the core at the centre of the star becomes large enough that the star can no longer support itself through the pressure generated by the nuclear reaction. At this point the star will begin to implode. When the outer layers of the star impact the core, the energy of the collapse is released as an explosion, with a *supernova remnant* left behind. The exact nature of the remnant depends on the mass of the core; cores above 5 $M_\odot$ will turn into black holes, while cores with less mass will become neutron stars.

The energy released by different kinds of supernova explosions can vary by orders of magnitude. In this thesis I will assume a standard supernova energy of $E_{SN} = 10^{51}$ erg. This is within an order of magnitude of energy of a typical Type Ia supernova [Khokhlov et al. 1993], and the energy of a Type II supernova with an initial mass of 8 – 10 $M_\odot$ [Hillebrandt et al. 1984] which are estimated to account for around half of all observed Type II supernovae [Tammann et al. 1982]. I am purposefully conflating the types of supernova as the foundation that I am using for the supernova implementation represents whole stellar nurseries (see §4.2.1) and as such both types may be present.

2.1.3 The Structure of a Supernova

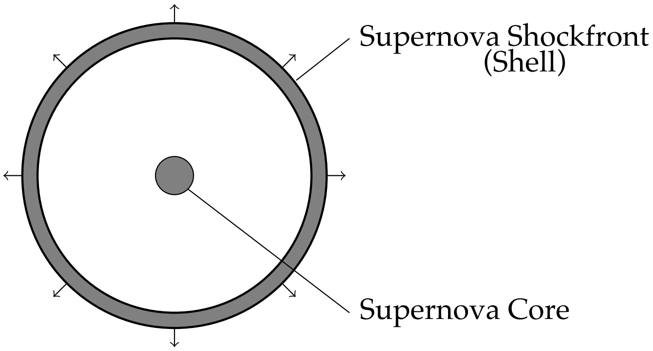

Figure 2.2: A diagram depicting the basic structure of a supernova explosion.

While, the structure of a supernova is fairly simple to understand (see Figure 2.2), the exact nature of the structure does depend on the stage of evolution that the supernova is in. There are three main stages of supernova evolution: the *free expansion phase*, the *Sedov phase*, and the *snowplow phase*.

The free expansion phase occurs immediately after the initial supernova explosion. It is very short lived, lasting on the order of a hundred years. The main characteristic of the free expansion phase is that the expanding shock is moving very fast, on the order of 10 000 km/s, and the expanding shell has yet to pick up any significant mass from the surrounding region, so it doesn't slow down.

Immediately after the free expansion phase the supernova enters the Sedov phase. This phase lasts significantly longer than the free expansion phase — on the order of a few hundred thousand years — during which the supernova shockfront expands significantly slower, on the order of 100–1000 km/s. The supernova itself at this point consists of a thin dense shell that is expanding supersonically into the surrounding medium as a shockwave. The majority of the energy contained within the shell is in the form of thermal energy with an extremely hot core. The remaining energy is located in the kinetic regime and is focussed in the shell, where the majority of the mass is located. This is the phase of supernova evolution that this thesis focusses on, and is discussed in far greater detail in §3.

After the Sedov phase has broken down, the supernova enters the final phase: the snowplow phase. Compared to the previous phases the snowplow phase is fairly timid. The majority of the energy in the supernova has been radiated away, with the supernova now being momentum-driven. The sharp shell that was present in the Sedov phase has now softened, with the outer portion of the shell cooling. The interior of the supernova is still hot, though it has cooled significantly at this stage.

2.2 Supernova-Driven Turbulence

Supernova-driven turbulence explicitly refers to turbulence that is generated as a result of a supernova, whether that be the injection of kinetic energy from the snowplow or Sedov phases, or the radiated energy heating up the surrounding gas. This by-product of the supernova evolution is the main aspect that the Supernova module will be used to examine, and determine the effects of this turbulence on the overall structure of the interstellar medium.

2.2.1 What is Turbulence?

The motion of a fluid is described by the field of *fluid dynamics*. The field itself has two sub-fields: *hydrodynamics*, or the study of the movement of liquids, and *aerodynamics*, the study of the movement of air and its interactions with solids. However, in practice the field of hydrodynamics is used to describe the movement of both liquids and gases as they share many common properties.

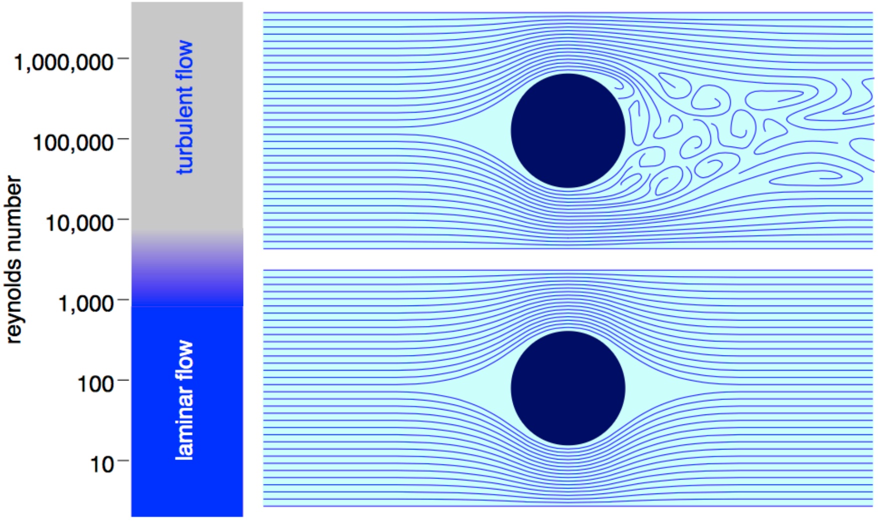

Figure 2.3: A figure depicting two different types of fluid flows: laminar and turbulent. [Image: Reynolds, SVG, 2016]

We refer to the movement of a liquid as a *flow*. There are two main types of flows: *steady flows* which do not change their internal properties over time, and *unsteady flows* which do. In practice this means that if we want to describe either type of flow with a set of questions we need to consider time for unsteady flows.

Equivalently, there are two other types of flows that are commonly referred to: *turbulent flows* and *laminar flows*. These are more or less equivalent to the previous terms, but with a few slight differences: all turbulent flows are unsteady flows, but not all unsteady flows are turbulent.

The difference between laminar and turbulent is clear upon a first examination of both. Figure 2.3 depicts a comparison between a laminar and a turbulent flow around the same object. The blue lines indicate the streamlines within the flow. Laminar flow is characterised by having smooth streamlines that are all parallel, while turbulent flow is characterised by the presence of swirling eddies and non-uniformity in the streamlines. Another visual exploration of turbulence can be found in the first chapter of [Frisch 1995].

Beyond the visual, there is also a numerical way to distinguish between the two kinds of flows: the degree to which a given flow is either laminar or turbulent can be quantified by the *Reynolds number*[Stokes 1851; Reynolds 1883].

$$\mathrm{Re} = \frac{vL}{\nu} \tag{2.4}$$

The Reynolds number, Re, for a given fluid flow is a dimensionless parameter that represents the ratio of the intertial forces within the flow to the viscous forces present within the fluid. This can be expressed as the ratio of the velocity of the flow, v, and the characteristic length, L, to the kinematic viscosity of the fluid, ν, as shown in (2.4). When this ratio is low then this means that the flow is typically slow moving, and is in a steady flow state. Higher Reynolds numbers are associated with turbulent flows; flows in which the inertial forces are significantly higher than the friction caused by the viscous forces.

From (2.4) we can also see that for identical conditions, e.g. the same characteristic length, and the same kinematic viscosity, the Reynolds number is proportional to the velocity of the flow, and hence the kinetic energy within the fluid. However, in reality this relationship is more complex as increased velocity can heat the fluid when considering compressive flows which in turn modifies the kinematic viscosity.

2.2.2 Types of Turbulent Driving

Turbulence can be introduced to a given fluid by *driving* it, inserting kinetic and internal energy that increase the inertial forces within the gas and hence the Reynold number for the flows. We begin by defining two main types of turbulent driving: *compressive*, and *solenoidal*. Solenoidal driving is divergence-free while compressive driving is curl-free [Federrath et al. 2008; Federrath et al. 2010].

The mechanisms of turbulent driving have been examined thoroughly in past studies. They can be broadly classified in terms of their sources, being classified as either stellar or dynamic [Federrath et al. 2016]. Stellar turbulence is the result of stellar phenomena such as jet outflows and accretion discs [Krumholz et al. 2006; Federrath et al. 2014], supernova shocks [Dubois and Teyssier 2008; Simpson et al. 2015], or ionisation fronts [McKee 1989]. Dynamic sources are results of gas dynamics, such as rotational or magneto-rotational instabilities [Piontek and Ostriker 2004; Piontek and Ostriker 2007], or galactic accretion [Klessen and Hennebelle 2010].

As supernovae represent a source of compressive forcing, this is the type of turbulent driving that I will be focussing on from this point on in the thesis.

2.2.3 The Role of Turbulence in Large Scale Evolution

The role that turbulence can play in the formation stars is best explained by recalling the relationship between the kinetic energy within the movement of the gas and the Reynolds number for that movement. A region with higher levels of turbulence also has higher amounts of kinetic energy within that region. We know from (2.2) that the mass limit for the start of the gravitational collapse that can form stars is dependent on the amount of kinetic energy within the region, via (2.1). Higher turbulence typically means higher velocities, see (2.4), so the threshold for gravitational collapse is higher is large scale is smaller [Federrath and Klessen 2012].

On the small scale, we have triggered star formation. This refers to a situation in which an event, such as a supernova, introduces a shock to the surrounding area. This shock compresses the gas as it propagates, and can cause the density of the gas to surpass the Jeans mass locally, or even cause star formation on its own.

These effects can be quantified by the *Star Formation Rate* (SFR). This is measure of the amount of gas that forms stars within a given time period. The standard units for the SFR is $M_\odot$ yr^{-1}. Equally, the star formation within a galactic cloud can be described through the use of the *Star Formation Efficiency* (SFE), given in (2.5). This is a measurement of the efficiency of the cloud at generating new stars and can intuitively be thought of as the amount of mass from the gas cloud that went into star formation as a fraction of the total mass of the cloud.

$$SFE = \frac{M_{star}}{M_{tot}} \tag{2.5}$$

The current observational estimates for the SFR in the Milky Way and nearby galaxies indicate that the SFE is lower than it would be under the naïve assumptions of classical gas dynamics, such as the galactic free-fall time. Current theories that explain the discrepancy put forth that the existence of supersonic turbulence within the gas cloud can help to regulate the SFR [Mac Low and Klessen 2004; Krumholz and McKee 2005; McKee and Ostriker 2007; Krumholz et al. 2009; Hennebelle and Chabrier 2011; Federrath and Klessen 2012; Padoan et al. 2014; Salim et al. 2015], and hence the SFE within the cloud.

Recent literature has found that the introduction of different kinds of turbulence can dramatically affect the measured SFR and SFE[Federrath and Klessen 2012]. Additionally, the inclusion of the turbulence generated by stars throughout their formation can significantly affect the measured SFR in simulations [Federrath et al. 2014]. A continuation of the work in this area will be one of the main uses of the products of this thesis.

Additionally, the observed structure of molecular gas clouds cannot be accurately described by formation from gravitational collapse alone. The observed velocity dispersions indicate the present of significant internal turbulent motion [Larson 1981]. Different forms of turbulent driving has also been shown to affect the density fluctuations within a molecular cloud, with compressive driving producing a standard deviation from the mean 3 times larger than equivalent solenoidal forcing [Federrath et al. 2008; Federrath et al. 2010], and impacts the proportion of gas within high density regions [Kainulainen et al. 2013]

2.3 Numerical Methods for Hydrodynamic Simulations

In practice it is difficult to find analytical forms for complex physical systems, especially ones involving numerous interlinked physical processes. Due to the chaotic and apparent random nature of highly turbulent flows accurately modelling them with analytical functions is an intractable problem given the complex interplay of the kinematic viscosity, temperature, density, compressions, etc.

The resolution of this issue is to use numerical methods to model the evolution of the gas or turbulent flow in a set of simulations that can be minutely controlled.

2.3.1 FLASH

Accurately simulating a physical phenomenon requires simulating a variety of physical interactions. For example, simulating a supernova requires simulating the movement of gas, kinetic and internal energy conversion resulting from the compression of gas, and cooling.

In order to avoid recoding basic physical interactions, codebases have been developed that simulate the majority of the requirements for typical simulations. These codebases can then be used and adapted to suit any requirements of an individual simulation. FLASH is one such codebase.

FLASH is an Eulerian, grid-based, hydrodynamics simulation code. FLASH was first released in 2000 by the Center for Astrophysical Thermonuclear Flashes, or 'Flash Center', in association with the University of Chicago [Fryxell et al. 2000]. It was designed to be easily extendable, employing a modular design that enables users to develop their own modules that can be inserted into the codebase and automatically integrate with the rest of the code. This is implemented using a hierarchy in which submodules are able to inherit the properties of their parent-module.

2.3.2 Hydrodynamic Solvers

Hydrodynamic solvers form the basis of hydrodynamical simulations, by determining the numerical solution to the movement and interaction of gas in the simulation box. They do this by numerically solving a provided set of differential equations that govern the movement and conservation of the mass, momenta, and pressure of the gas. The standard equations that are used include the Euler equation, and the continuity equations. These differential equations will also be *closed* by the inclusion of an *equation of state* [Gallagher 2012] that encodes the relationship between the pressure, density, and temperature of the gas.

2.3.3 Types of Hydrodynamic Solvers

FLASH classifies hydrodynamic solvers into two main kinds: *split*, and *un-split*. The difference between the two classifications comes down to how they treat their time-steps. A split solver will take two half-steps for each major time-step, while an un-split solver will only take the one step. A split solver does this to ensure the *time-reversibility* of the resulting solution.

One of the fundamental laws of physics is the conservation of energy; energy can neither be created nor destroyed. One of the pre-eminent results of mathematical physics in the 20th century was the discovery that this conversation law was in fact the result of the *time symmetry* of physics [Noether 1918] — physical interactions are reversible. The result of this is that in order to ensure complete energy conservation a numerical solver must also ensure time-symmetry in its solution. A good example of the use of this symmetry are the symplectic group of numerical solvers, such as the leapfrog solver [Hockney and Eastwood 1988], that are used in simulations that require strict conservation of energy over a long period of time.

Split hydrodynamic solvers take the requirement of time-reversibility and apply it to the method in which they propagate the solution of the conservational equations. For a given timestep, dt, the solver implements two half-steps of length $\frac{dt}{2}$. Within the first half-step the solver solves the differential equations in each cardinal direction sequentially, propagating the gas each time. In the second half-step this process is repeated, but with the order of evaluation reversed. This ensures that the time-step as a whole is the same when viewed forwards and backwards, thus satisfying the time-reversibility requirement.

Un-split solvers, however, use other methods to ensure symmetries. However, the methods used are outside the scope of this thesis so I will not go into them.

2.3.4 Bouchut Solvers

FLASH implements the Bouchut series of hydrodynamic solvers[Bouchut et al. 2010; Waagan et al. 2011]. They are able to simulate magnetohydrodynamics (MHD) evolution as well as regular hydrodynamics. This is achieved by adding the magnetic induction equation to the existing equations for a typical hydrodynamic solver, and ensuring that Maxwell's equations hold, i.e. $\nabla \cdot B = 0$. The existing also have to be modified to account for the existence of magnetic pressure and tension within the simulation.

FLASH has two main branches of the Bouchut solvers, **bouchut3** and **bouchut5** corresponding to the 3 and 5 wave solutions put forth by Bouchut. Within the bouchut3 branch there are solvers for the ideal, polytropic, and isothermal equations of state, referred to as **bouchut3**, **bouchut3_polytropic**, and **bouchut3_isothermal** respectively. These are the solvers that I use for this thesis.

The Bouchut solvers use the provided equation of state to ensure conservation within the simulation. During each time-step they will overwrite the pressure, or internal energy values within a given cell to ensure that the relationship provided by the equation of state within each of the cells is enforced. For the simulations that I run in this thesis, the Bouchut solvers overwrite the pressure.

2.3.5 Convergence Conditions for Numerical Methods

While there are many different methods that can be used to solve the set of differential equations, such as the method of finite differences, different Riemann solvers, or Adam's method, we need to ensure that whatever method is chosen that the resulting solution is stable. The classic solution for this problem is to employ the Courant-Friedrichs-Lewy (CFL) condition for converging solutions of partial differential equations [Courant et al. 1967]. This provides an upper limit for the time-step of the solution that is necessary for the stability of the solution.

$$dt \leq \frac{C_{CFL}\Delta x}{\dot{x}} \tag{2.6}$$

The maximum allowable time-step is given by (2.6). This can intuitively be thought of as ensuring that the maximum allowable time-step is less than the time it would take for something moving at a speed of $\dot{x}$ to traverse the width of a given cell Δx, then scaled by the Courant number, C_{CFL}. In order to ensure stability we require $C_{CFl} \leq 1$, though typically values of $C_{CFL} \leq 0.5$ are used to ensure convergence. For a given simulation the maximum-allowable time-step is the global spatial minimum of the time-step given by the CFL condition.

The CFL condition can also be calculated for a variety of different physical in a simulation. While I have only mentioned the velocity analogue above, it is also possible to apply the CFL condition to the calculation of the speed of a magnetic wave, i.e. in an magnetohydrodynamics solver such as the Bouchut solvers, or to define analogues such as the maximum allowable temperature change, see §4.11.

Chapter 3

The Sedov Solution

In this chapter I present an overview of the Sedov blast wave solution. I begin with a brief overview of the history of the solution, before presenting a full derivation of the solution. I also present an examination of the conditions under which the assumptions made by the Sedov solution break down.

3.1 Background

The Sedov solution is named for Leonid Sedov, a Soviet physicist from mid-twentieth century. Sedov was one of the pioneers of the use of similarity and dimensional analysis to solve physical problems. He is possibly most well-known for his book 'Similarity and Dimensional Methods in Mechanics' which he initially published in the USSR in 1944. The manual then went on to be published in over 10 different languages, and in multiple versions throughout the following decades.

In this book, Sedov outlines a self-similar solution for a blast-wave generated by a point explosion in a medium of constant density [Sedov 1959]. This solution found widespread use throughout the 20th century and beyond as a method for analysing the effect of explosions. It has also found use within the astrophysics community as a method for describing one of the major phases of supernova evolution. This solution has become a keystone for the field of simulating supernovae as it provides a clear analytical profile that simulations can be compared to.

3.2 Derivation

3.2.1 Assumptions of the Sedov Solution

In this section I outline the main assumptions behind the Sedov solution. First we assume that the initial influx of energy is high enough to make the expansion speed of the resulting shock supersonic; this ensures that the resulting shock is *strong* and allows us to make key simplifications later in the derivation. We also assume that the sudden influx of energy occurs at a single point at the centre of the resulting shock so the expanding shock is spherical.

There are a host of other assumptions that are necessary for the derivation of the Sedov solution as well as for determining if the solution is valid for a set of physical conditions. I will briefly cover the assumptions here, and cover them in detail as they become important later in this thesis.

3.2.1.1 List of Physical Assumptions

- **Pressure**: we assume that the internal pressure is significantly higher than the pressure of the external medium
- **Energy Conservation**: we assume that the amount of energy that is radiated from the expanding shock is significantly less than the injected energy, meaning that the energy is constant.
- **Background Medium**: we assume that the background medium that the shock is inserted into is cold, stationary relative to the shock, and has a uniform density.

3.2.2 Initial Conditions

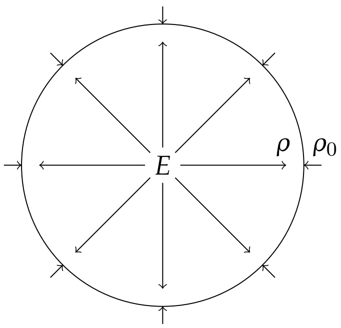

Figure 3.1

Consider a sudden influx of some finite amount of energy, E, into a point within a cold stationary medium of constant density, ρ_0, with an adiabatic constant of γ. The sudden influx causes a shock wave that expands uniformly into the background medium.

Values for the density, pressure, and velocity of gas inside the expanding shock can be calculated using the Rankine-Hugoniot jump conditions[Rankine 1870; Hugoniot 1887], given by

$$\frac{\rho_0}{\rho} = \frac{\gamma-1}{\gamma+1} + \frac{2}{(\gamma+1)\mathcal{M}_1^2} \tag{3.1}$$

$$\frac{v}{v_0} = \frac{\gamma-1}{\gamma+1} + \frac{2}{(\gamma+1)\mathcal{M}_1^2} \tag{3.2}$$

$$\frac{P}{P_0} = \frac{2\gamma\mathcal{M}_1^2}{\gamma+1} - \frac{\gamma-1}{\gamma+1}. \tag{3.3}$$

where $\mathcal{M}_1$ denotes the Mach number of the shock, $\mathcal{M}_1 = \frac{v_0}{c_s}$. Note that these conditions are listed in the frame of reference of the shock. As such v_0 denotes the velocity of the external medium with respect to the shock, and is therefore non-zero.

If the input energy is sufficiently high — as it is in an explosion — then the resulting shock can be thought of as a *strong* shock. This means that the shock is expanding with a velocity that is much greater than the speed of sound in the external medium, i.e. $\mathcal{M}_1 \gg 1$. This allows the Rankine-Hugoniot jump conditions to be simplified to the following

$$\frac{\rho_0}{\rho} = \frac{\gamma-1}{\gamma+1} \tag{3.4}$$

$$\frac{v}{v_0} = \frac{\gamma-1}{\gamma+1} \tag{3.5}$$

$$P = \frac{2\rho_0 v_0^2}{\gamma+1}. \tag{3.6}$$

The change to the pressure equation can be explained as follows. The external pressure, P_0, can be expressed as

$$P_0 = \frac{\rho_0 c_s^2}{\gamma}. \tag{3.7}$$

Substituting this into (3.3) yields

$$P = \frac{2\gamma\mathcal{M}_1^2}{\gamma+1}\frac{\rho_0 c_s^2}{\gamma} - \frac{\gamma-1}{\gamma+1}\frac{\rho_0 c_s^2}{\gamma} = \frac{2\rho_0 v_0^2}{\gamma+1} - \frac{\gamma-1}{\gamma+1}\frac{\rho_0 c_s^2}{\gamma}. \tag{3.8}$$

We then employ the strong shock assumption ($\mathcal{M}_1 \gg 1 \implies v_0 \gg c_s$) and recover (3.6) as required.

In order to continue with the solution it is necessary to change the frame of reference of the equations from the shock to the external medium. This will only affect the velocity terms, yielding new terms v_{int} and v_{ext} for the velocities inside and outside the shock respectively. They are given by

$$v_{\text{ext}} = v_s - v_0 \tag{3.9}$$

$$v_{\text{int}} = v_s - v \tag{3.10}$$

with the velocity of the shock itself given by v_s. Noting that our original assumption requires a stationary external gas we have that $v_{\text{ext}} = 0$ which implies that $v_s = v_0$. We can then substitute in a value for v using (3.5), yielding

$$v_{int} = v_s - \frac{\gamma - 1}{\gamma_1} v_s = \frac{2}{\gamma + 1} v_s. \tag{3.11}$$

Using this expression we can now write down expressions for the density, pressure, and velocity inside the expanding shock as follows

$$\rho = \frac{\gamma + 1}{\gamma - 1} \rho_0 \tag{3.12}$$

$$v = \frac{2}{\gamma + 1} v_s \tag{3.13}$$

$$P = \frac{2}{\gamma + 1} \rho_0 v_s^2 \tag{3.14}$$

3.2.3 Deriving the Self-Similarity Variable

One of the strengths of the Sedov solution is that it is a self-similar solution. This means that the solution can be characterised in terms of a dimensionless variable — which we will denote henceforth as η — in the coordinate system where the solution is stationary. To put this more simply, the solution looks the same regardless of the physical size or evolutionary stage of the expansion, and is constant when expressed in terms of η.

As seen in (3.12) – (3.14) we can calculate any of the required variables by using just the external density and the expansion speed of the shock. Further, the speed of the shock depends on three variables: the radius of the shock, the age of the shock, and the initial energy. The radius and time are easily explained as velocity is the rate of change of the radius with respect to time, i.e. $v = \frac{dr}{dt}$, or $v \approx \frac{r}{t}$. The energy dependence can be intuitively explained by considering that higher energy explosions would expand faster than lower energy explosions.

Under these assumptions we wish to determine a dimensionless variable η as a combination of r, t, E, and ρ. The dimensionality of each of these variables in terms of length, L, time, T, and mass, M, is given by

$$[r] = L \tag{3.15}$$

$$[t] = T \tag{3.16}$$

$$[E] = \frac{ML^2}{T^2} \tag{3.17}$$

$$[\rho] = \frac{M}{L^3} \tag{3.18}$$

We assume that η will be given by some product of our four variables as follows

$$[\eta] = r^j t^k E^l \rho^m. \tag{3.19}$$

Substituting in the dimensionalities given by (3.15) – (3.18) produces

$$\eta = L^{j+2l-3m} T^{k-2l} M^{l+m} \tag{3.20}$$

This is equivalent to the following set of linear equations

$$j + 2l - 3m = 0 \tag{3.21}$$

$$j - 2l = 0 \tag{3.22}$$

$$l + m = 0 \tag{3.23}$$

This has a solution given by $j = 1, k = -\frac{2}{5}, l = -\frac{1}{5}, m = \frac{1}{5}$. Hence, we can express η as

$$\eta = r \left(\frac{\rho}{Et^2} \right)^{\frac{1}{5}}, \tag{3.24}$$

or alternatively we can express the position of the shock at any time for a given external density and initial energy as

$$r = \eta \left(\frac{Et^2}{\rho} \right)^{\frac{1}{5}}. \tag{3.25}$$

I will refer to this process of determining r as 'redimensionalising' from here on.

As the solution is constant in η we will denote the position of shock in the η coordinate system by η_s. We can then determine the radius of the shock using

$$r_s = \eta_s \left(\frac{Et^2}{\rho} \right)^{\frac{1}{5}} \tag{3.26}$$

Note at this point that I am using r_s to denote the shock position as I am presenting a generalised solution for blast-waves. In later sections of this thesis — where I am discussing supernovae specifically — I will use r_{SN} to denote the radius of the shock, however the equation will remain the same.

3.2.4 Creating Ansätze and Solving the Euler Equation

In order to proceed with the Sedov solution we will now make a series of 3 ansätze based on (3.12) – (3.14).

$$\rho(r,t) = \frac{\gamma+1}{\gamma-1} \rho_0 A(\eta) \tag{3.27}$$

$$P(r,t) = \frac{2}{\gamma+1} \rho_0 v_s \left(\frac{\eta}{\eta_s} \right)^2 B(\eta) \tag{3.28}$$

$$v(r,t) = \frac{2}{\gamma+1} v_s \left(\frac{\eta}{\eta_s} \right) C(\eta). \tag{3.29}$$

Here $r \leq r_s$, and we assume that $A(\eta_s) = B(\eta_s) = C(\eta_s) = 1$, thereby recovering (3.12) – (3.14) at the position of the shock.

The next step in the derivation requires us to solve the hydrodynamical equations for a spherical coordinate system. These equations are:

$$\frac{\partial}{\partial t}\rho + \frac{1}{r^2}\frac{\partial}{\partial r}(r^2 v\rho) = 0 \tag{3.30}$$

$$\frac{\partial}{\partial t}v + v\frac{\partial}{\partial r}v + \frac{1}{\rho}\frac{\partial}{\partial r}P = 0 \tag{3.31}$$

$$\frac{\partial}{\partial t}\left[\frac{P}{\gamma-1} + \frac{1}{2}\rho v^2\right] + \frac{1}{2}r^2\frac{\partial}{\partial r}\left[r^2 v\left(\frac{P}{\gamma-1} + P + \frac{1}{2}\rho v^2\right)\right] = 0. \tag{3.32}$$

We now need to perform a change of basis to put these equations explicitly in terms of η. The required change of basis is,

$$\left.\frac{\partial}{\partial t}\right|_r \mapsto \left.\frac{\partial \eta}{\partial t}\right|_r \left.\frac{\partial}{\partial \eta}\right|_t + \left.\frac{\partial t}{\partial t}\right|_r \left.\frac{\partial}{\partial t}\right|_\eta \tag{3.33}$$

$$\left.\frac{\partial}{\partial r}\right|_t \mapsto \left.\frac{\partial \eta}{\partial r}\right|_t \left.\frac{\partial}{\partial \eta}\right|_t + \left.\frac{\partial t}{\partial r}\right|_t \left.\frac{\partial}{\partial t}\right|_\eta \tag{3.34}$$

Using (3.24) we can evaluate the partial derivatives of η to produce the final expressions for the change of basis

$$\left.\frac{\partial}{\partial t}\right|_r \mapsto -\frac{2\eta}{5t}\left.\frac{\partial}{\partial \eta}\right|_t + \left.\frac{\partial}{\partial t}\right|_\eta \tag{3.35}$$

$$\left.\frac{\partial}{\partial r}\right|_t \mapsto \frac{\eta}{r}\left.\frac{\partial}{\partial \eta}\right|_t \tag{3.36}$$

Substituting these into (3.30) – (3.32) yields

$$\frac{\partial \rho}{\partial t} - \frac{2\eta}{5t}\frac{\partial \rho}{\partial \eta} + \frac{\eta}{r^3}\frac{\partial}{\partial \eta}(r^2 v\rho) = 0 \tag{3.37}$$

$$\frac{\partial v}{\partial t} - \frac{2\eta}{5t}\frac{\partial v}{\partial \eta} + \frac{v\eta}{r}\frac{\partial v}{\partial \eta} + \frac{\eta}{r\rho}\frac{\partial P}{\partial \eta} = 0 \tag{3.38}$$

$$\left(\frac{\partial}{\partial t} - \frac{2\eta}{5t}\frac{\partial}{\partial \eta}\right)\left[\frac{P}{\gamma-1} + \frac{1}{2}\rho v^2\right] + \frac{\eta r}{2}\frac{\partial}{\partial \eta}\left[r^2 v\left(\frac{P}{\gamma-1} + P + \frac{1}{2}\rho v^2\right)\right] = 0 \tag{3.39}$$

Having found the conservation equations in terms of η we can now substitute in our ansätze to produce the following set of coupled differential equations:

$$-\eta\frac{dA}{d\eta} + \frac{2}{\gamma+1}\frac{d}{d\eta}(\eta AC) + \frac{4}{\gamma+1}AC = 0 \tag{3.40}$$

$$-C - \frac{2}{5}\eta\frac{dC}{d\eta} + \frac{4}{5(\gamma+1)}\left(C^2 + C\eta\frac{dC}{d\eta}\right) + \frac{2}{5}\frac{\gamma-1}{\gamma+1}\frac{1}{A}\left(2B + \eta\frac{dB}{d\eta}\right) = 0 \tag{3.41}$$

$$-2(B+AC^2) - \frac{2}{5}\eta\frac{d}{d\eta}(B+AC^2) + \frac{4}{5(\gamma+1)}\left(5C(\gamma B + AC^2) + \eta\frac{d}{d\eta}[C(\gamma B + AC^2)]\right) = 0. \tag{3.42}$$

From this set of coupled differential equations we can then determine a set of explicit differential equations for each of our ansatz functions: A, B, and C. Solving this set of equations yields the complete Sedov solution, describing the radial profiles of the density, pressure, and velocity for the blast wave.

3.2.5 Generating Radial Profiles

While an analytical solution for (3.40) – (3.42) is possible, from this point in the derivation it is easier to perform a numerical integration. As such, this is the process that I use for solving the equations in my code.

In order to perform a numerical integration we require a starting point at which the value for the function to be integrated is known. In this case our ansätze provide this point with the assumption that $A(\eta_s) = B(\eta_s) = C(\eta_s) = 1$. However, a value for η_s has never been explicitly given throughout the derivation. This is because the value of η_s depends on γ — i.e. the 'stiffness' — of the medium into which the blast-wave is expanding.

This is where we use the assumptions made in Section 3.2.1, particularly the assumption that the Sedov solution is an energy conserving system. As such we can determine the total energy within the blast-wave at any point throughout its evolution and the result will always be the same. This can be formalised by

$$\int_0^{r_s}\left(\frac{P(r)}{\gamma-1} + \frac{1}{2}\rho(r)v(r)^2\right)4\pi r^2\,dr = E \tag{3.43}$$

where E is the energy that was initially put into the system. Using (3.27) – (3.29) we can transform this integral as follows

$$\begin{aligned}
E &= \int_0^{r_s} \left(\frac{P(r)}{\gamma - 1} + \frac{1}{2}\rho(r)v(r)^2 \right) 4\pi r^2 \, dr \\
&= 4\pi \int_0^{r_s} \left(\frac{2\rho_0 v_s^2}{\gamma^2 - 1} \left(\frac{\eta}{\eta_s} \right)^2 B(\eta) + \frac{1}{2} \left(\frac{\gamma + 1}{\gamma - 1} \rho_0 A(\eta) \right) \left(\frac{2}{\gamma + 1} v_s \left(\frac{\eta}{\eta_s} \right) C(\eta) \right)^2 \right) r^2 \, dr \\
&= 4\pi \int_0^{r_s} \left(\frac{2\rho_0 v_s^2}{\gamma^2 - 1} \left(\frac{\eta}{\eta_s} \right)^2 B(\eta) + \frac{2\rho_0 v_s^2}{\gamma^2 - 1} \left(\frac{\eta}{\eta_s} \right)^2 A(\eta)C(\eta)^2 \right) r^2 \, dr \\
&= \frac{8\pi\rho_0 v_s^2}{\gamma^2 - 1} \int_0^{r_s} \left(B(\eta) + A(\eta)C(\eta)^2 \right) \left(\frac{\eta}{\eta_s} \right)^2 r^2 \, dr
\end{aligned}$$

We can then use (3.25) to remove the r dependence of the integral and put it in terms of our dimensionless variable. Formulating the integral in terms of η means that we are able to integrate this from known boundaries at all points, and allows us to determine fundamental properties about the energy distribution of the Sedov solution. We perform the following change of variables for the integral

$$dr \mapsto d\eta \left(\frac{Et^2}{\rho_0} \right)^{\frac{1}{5}}, \quad r_s \mapsto \eta_s, \quad 0 \mapsto 0. \tag{3.44}$$

This yields an integral of

$$\begin{aligned}
E &= \frac{8\pi\rho_0 v_s^2}{\gamma^2 - 1} \frac{1}{\eta_s^2} \int_0^{\eta_s} \left(B(\eta) + A(\eta)C(\eta)^2 \right) \eta^4 \left(\frac{Et^2}{\rho_0} \right)^{\frac{3}{5}} d\eta \\
&= \frac{8\pi\rho_0 v_s^2}{\gamma^2 - 1} \frac{1}{\eta_s^2} \left(\frac{Et^2}{\rho_0} \right)^{\frac{3}{5}} \int_0^{\eta_s} \left(B(\eta) + A(\eta)C(\eta)^2 \right) \eta^4 \, d\eta
\end{aligned}$$

To proceed further we note that $v_s = \frac{dr_s}{dt}$ and therefore

$$v_s = \frac{d}{dt}\eta_s \left(\frac{Et^2}{\rho_0} \right)^{\frac{1}{5}} = \frac{2\eta_s}{5} \left(\frac{E}{\rho_0 t^3} \right)^{\frac{1}{5}} \tag{3.45}$$

Substituting this expression into the integral produces:

$$\begin{aligned}
E &= \frac{32\pi\rho_0}{25(\gamma^2 - 1)} \left(\frac{E}{\rho_0 t^3} \right)^{\frac{2}{5}} \left(\frac{Et^2}{\rho_0} \right)^{\frac{3}{5}} \int_0^{\eta_s} \left(B(\eta) + A(\eta)C(\eta)^2 \right) \eta^4 \, d\eta \\
&= \frac{32\pi\rho_0}{25(\gamma^2 - 1)} \frac{E}{\rho_0} \int_0^{\eta_s} \left(B(\eta) + A(\eta)C(\eta)^2 \right) \eta^4 \, d\eta
\end{aligned}$$

Therefore our energy integral in terms of η is given by

$$\frac{32\pi}{25(\gamma^2-1)}\int_0^{\eta_s}\left(B(\eta)+A(\eta)C(\eta)^2\right)\eta^4\,d\eta = 1. \tag{3.46}$$

Using this integral we can determine whether or not our chosen starting point for the numerical integration, η_s, was correct by taking the generated profiles, evaluating this integral and seeing how close the integral approaches unity. If the integral evaluates to more than 1, then η_s needs to be scaled down, evaluating to less than 1 implies η_s needs to be scaled up. For a gas with $\gamma = \frac{5}{3}$ we have $\eta_s \approx 1.15$.

A plot of the normalised profiles generated by this method can be found in Figure 3.2.

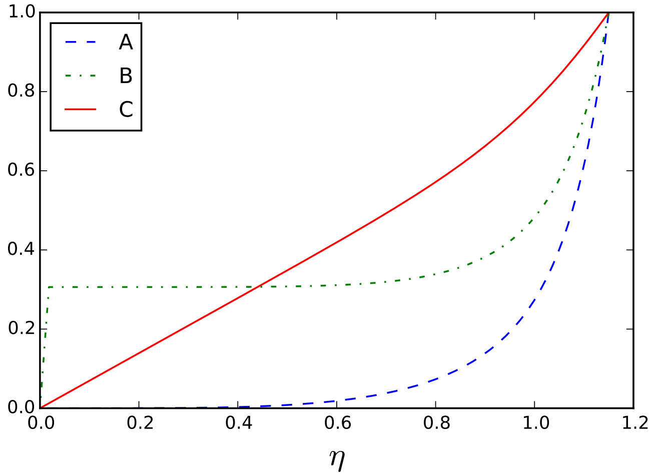

Figure 3.2: The normalised profiles produced by the Sedov solution for $\eta_s = 1.15$. Definitions for A, B, and C can be found in (3.27)–(3.29), and correspond to the density, pressure, and velocity profiles respectively.

3.3 Defining the End of the Sedov Solution

The following section is based on a derivation of the lifetime of the Sedov solution performed in [Ryden 2011].

As stated in §3.2.1 there are two main assumptions that we make when initially defining the Sedov solution. These are that the pressure inside the shock is much higher than the pressure of the external medium, and that the radiated energy is significantly smaller than the injected energy. If we violate either of these assumptions we can conclude that the Sedov solution is no longer valid at this point. Given the expression for pressure in (3.14) we can easily calculate the regime in which the Sedov solution will no longer be valid.

Using the definition of the supernova radius at time t we can determine an expression for the shock speed, v_s, by noting that

$$v_s = \frac{dr_s}{dt} = \frac{d}{dt}\eta_s \left(\frac{Et^2}{\rho_0}\right)^{\frac{1}{5}} = \frac{2}{5}\eta_s \left(\frac{E}{\rho_0 t^3}\right)^{\frac{1}{5}}.$$

Substituting this expression into (3.14) yields the following expression for the pressure just inside of the expanding shock as a function of the time.

$$\begin{aligned} P &= \frac{2}{\gamma+1}\rho_0 v_s^2 \\ &= \frac{8}{25(\gamma+1)}\rho_0 \eta_s^2 \left(\frac{E}{\rho_0 t^3}\right)^{\frac{2}{5}} \\ &= \frac{8}{25(\gamma+1)}\eta_s^2 \rho_0^{\frac{3}{5}} E^{\frac{2}{5}} t^{-\frac{6}{5}} \end{aligned}$$

We can solve this for the time as a function of the shock pressure, yielding

$$t = \frac{8}{25(\gamma+1)}\eta_s^2 \rho_0^{\frac{1}{2}} E^{\frac{1}{3}} P^{-\frac{5}{6}}. \tag{3.47}$$

The break down of the pressure assumption will occur when the internal pressure of the shock is comparable to the external pressure. For a given density of 1 cm^{-3}, at a temperature of 10 K, the pressure of an ideal gas is $P = 1.38e \times 10^{-15}$ dynes cm^{-2}. Substituting in these values to (3.47) yields a characteristic time of

$$t = 1.24\,\text{Myr}\left(\frac{n}{1\,\text{cm}^{-3}}\right)^{\frac{1}{2}} \left(\frac{E}{10^{51}\,\text{erg}}\right)^{\frac{1}{3}} \left(\frac{P}{1.38\times 10^{-15}\,\text{dyne cm}^{-2}}\right)^{-\frac{5}{6}}. \tag{3.48}$$

This shows that the Sedov regime has a very long lifetime (~1 Myr) in typical interstellar conditions. But this is only one of the conditions that control the lifetime as we still need to examine the radiated energy.

The amount of energy that a cloud of gas, or a shock, radiates depends on two factors: the temperature of the gas, and the density of the gas. A combination of both of these values determines the cooling function that can be applied to the shock, allowing a calculation of the luminosity of the shock, and hence the amount of thermal energy that the shock will radiate in a given period of time.

Before proceeding with the analysis of the radiating condition we first want to determine an expression for the temperature of the expanding shock as a function of time. This can be done by first noting the ideal gas equation:

$$\frac{\partial P}{\partial \rho} = c_s^2 = \frac{\gamma k T}{\overline{m}} \tag{3.49}$$

where $\overline{m}$ is the average molecular mass of the gas in question, and k is the Boltzmann constant. Here we make the assumption that $\frac{\partial P}{\partial \rho} \approx \frac{P}{\rho}$, thus allowing us to solve for the temperature, producing:

$$T = \frac{P\overline{m}}{\gamma \rho k} \tag{3.50}$$

Finally, we can substitute in the definitions for the pressure and density just inside the shock, given in (3.12) and (3.14). This produces

$$T = \frac{8(\gamma - 1)}{25\gamma(\gamma + 1)^2} \frac{\overline{m}}{k} \rho_0^{-\frac{2}{5}} E^{\frac{2}{5}} t^{-\frac{6}{5}}. \tag{3.51}$$

For this analysis, rather than determining the time that the supernova will take to reach a given temperature, we instead want to figure out a characteristic time for the amount of radiated energy to be a sign of the violation of the energy conservation assumption.

After a period of 100 kyr, for the same physical values used in the previous simulation, we get the following value for the temperature of the supernova:

$$T = 1.8 \times 10^5 \text{ K} \left(\frac{\overline{m}}{1.037 \times 10^{-24} \text{ g}} \right) \left(\frac{n}{1 \text{ cm}^{-3}} \right)^{-\frac{2}{5}} \left(\frac{E}{10^{51} \text{ erg}} \right)^{\frac{2}{5}} \left(\frac{t}{10^5 \text{ yr}} \right)^{-\frac{6}{5}} . \tag{3.52}$$

Based on the value of the Sutherland-Dopita cooling curve [Sutherland and Dopita 1993] at this temperature, $\Lambda \approx 10^{-21}$ erg cm^{-3} s^{-1}, we can conclude that at this time the amount of radiated energy from the supernova (assuming a uniform temperature throughout the supernova shock) is on the order of 10^{51} erg. This is equivalent to the amount of energy that was originally inserted by the supernova, and hence would violate the assumption that the radiated energy was much less than the energy within the shock.

Based on these results we can see that the time taken for the expanding shock wave to radiate away the majority of the inserted energy is an order of magnitude smaller than the time it would take for the pressure assumption to be violated. As such we can conclude that the Sedov solution for a supernova will typically break down due to the loss of thermal energy within 100 kyr.

Chapter 4

Development of the Supernova Module

In this chapter I will present the development process of the Supernova module. I will begin with a short discussion of my design philosophy regarding the implementation of the module, before introducing the reader to the work that I use as a foundation for this work. Finally, I will cover the process of testing and refining the implementation to bring it in line with the original design philosophy.

4.1 Design Philosophy

My main motivation for this code — aside from the research applications — was to make the code as flexible and adaptable as possible. Any parameter that can be modified to change the conditions of a simulation must be available for a user to set. Secondarily, I wanted to limit the amount of hardcoded information in the module so that the Sedov solution can be generated dynamically depending on the needs of the simulation or the user in question.

Finally, I wanted this code to maintain as much of the analytical Sedov solution as is possible within the constraints of a simulation. Many previous Supernova implementations use less detailed approaches, making assumptions about the initial distribution of energy or inserting uniform distributions of the supernova quantities over a set volume [Dubois and Teyssier 2008; Simpson et al. 2015; Bubel 2016]. However, since the main phase of supernova evolution is the Sedov phase, it makes sense to use the Sedov solution initially rather than rely on the input solution approaching the Sedov phase over time.

4.2 Dependence on Prior Work

Because I am implementing the supernova module in FLASH I am able to build the solution and simulations around the pre-existing modules and hydro-solvers. The main foundations that I will dicuss here is are ‘Sink Particles’. A discussion of FLASH and the hydrodynamic solvers I use can be found in §2.3.1 and §2.3.4.

4.2.1 Sink Particles

Sink Particles (SP) are part of a method that was first developed as a means of alleviating regions of high density in numerical simulations [Bate et al. 1995]. These regions would often severely limit the global time-step, in turn introducing a significant barrier to effectively simulating the regions of stellar collapse and formation. Instead of simulating the increased density, creating a SP allows any excess density in the region to be accreted onto this particle without significantly changing the overall physics of the simulation [Federrath et al. 2010].

Beyond this computational advantage SPs also offer a physical analogue to star formation. It is well known that star formation occurs multiple times in parallel within a given star formation region, accounting for the formation and existence of stellar nurseries [Lada and Lada 2003]. Instead of resolving individual stars, a SP can be used to model the formation of a cluster of stars that form at the same time.

Due to the similar nature of SP and stars, we can essentially treat an SP as though it were itself a star. The FLASH implementation of SPs form accretion discs during their formation and also generate magnetic outflow jets under this assumption [Federrath et al. 2010; Federrath et al. 2014]. In this paper I further this relationship by using SP as the basis for my supernova module. Once a SP reaches a certain age and size it completes its life-cycle by triggering a supernova.

4.3 Generating the Sedov Profiles

Rather than employing a static set of Sedov profiles for a gas with a single adiabatic constant, I instead opted to dynamically generate the profiles and η_s at the start of each simulation based on a user set parameter, **sink_supernova_gamma**. The profiles are generated by numerically integrating the explicit differential equations obtained by solving (3.40) – (3.42). The numerical integration is performed using the 4th-order Runge Kutta method with an initial guess of $\eta_s = 1.01$[1].

Once the Sedov profiles have been generated, the convergence is checked using (3.46). If the convergence check is less than the required value of 1, then the value of η_s is incremented, and conversely if the value is greater than 1, then η_s is decremented. Each time we switch from incrementing (decrementing) to decrementing (incrementing) we also halve the increment (decrement) value. This ensures that the integral will eventually reach convergence to within the required tolerance. The tolerance can be set using the parameter **sink_supernova_tol**.

Once the profiles have been generated, they are then saved in arrays until the end of the simulation.

---

[1] This is set to slightly above 1, as the Sedov solution equations break down under the isothermal assumption $\gamma = 1$.

4.3.1 Sampling Rates

One important decision for numerical integration is the size of the spacing between integration points. If the spacing between the integration points is too large then information or stability can be lost when solving the differential equations. Conversely if the spacing is too small then computational time is lost by over-specifying the results. For the purposes of this module the integration points also serve as sampling points for the generated profiles.

Because of the shapes of the traditional Sedov profiles I choose to utilise a non-uniform sampling method. The set of n sampling points that are used can be described by:

$$\Omega_n = \left\{ \eta_s \left(1 - \frac{x^2}{(n-1)^2} \right) \middle| x \in \mathbb{Z}_n \right\}. \tag{4.1}$$

This produces a set of sampling points that are spaced closer together as they approach the limit of the supernova solution. This has two main advantages. First, it allows the numerical integration to be initially more stable as the separation of the points is smaller during the initially high slopes of the profiles, such as the Sedov density profile seen in Figure 4.1. Second, it allows the introduction of the solution into the simulation to be more accurate.

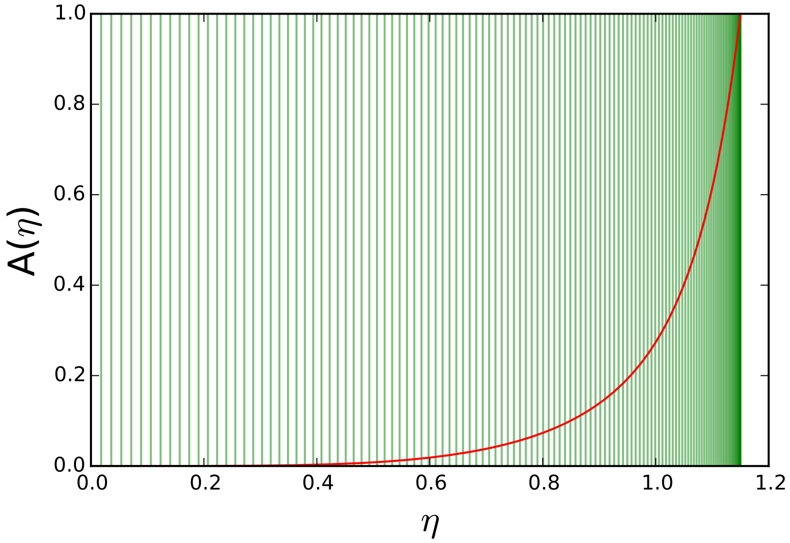

Figure 4.1: A plot showing a set of 128 sampling points generated using (4.1) against the Sedov density profile, $A(\eta)$.

The increase in accuracy is due to the second function of the sampling points. They provide a set of points at which the profiles themselves are sampled. However, in order to determine a profile value at any radius within the supernova the code performs a linear interpolation between the two closest values. Hence, having the sampling points closer together for the steep portions of the profiles means that the change between any two sampling points is closer to linear, and hence will reduce the error when performing a linear interpolation.

4.4 Supernova Eligibility

There are three conditions that need to be fulfilled in order for a SP to become a supernova. I based these conditions on the physical requirements for stars to become supernovae — namely a mass and age requirement — and an additional condition that ensures the inserted solution occurs at a reasonable time after the triggering event. I will discuss these conditions in more detail below.

4.4.1 Mass Requirement

Not all stars become supernovae [Chandrasekhar 1935]. Stars with an initial mass less than 8 $M_\odot$, become white dwarves at the end of their lifetime rather than becoming supernovae[Weidemann and Koester 1983]. Whereas, stars with a mass between 8 and 10 $M_\odot$ produce the majority of the observed Type II supernovae[Hillebrandt et al. 1984].

To mirror this constraint I implemented a mass threshold that SP must achieve in order to become a supernova. This threshold is a user-set parameter to accommodate different simulation requirements — SPs often represent more than a single star so the threshold would have to reflect this. For this thesis I use $M_{\text{thresh.}} = 8\ \mathrm{M}_\odot$ as I am using the SPs represent a single star.

4.4.2 Age Requirement

The process of becoming a supernova is one of the last stages of the lifecycle of a star. Therefore simulations should consider the age of a SP before triggering the supernova process rather than rely on a simple mass requirement.

To simulate stellar evolution, I implemented a stellar lifetime check into the supernova criteria. A SP will not be able to go supernova until it has reached some minimum age that the user can set. For general simulations this would be set to the lifetime of an average supernova capable star. For the purposes of testing, I set this to be zero to allow SPs to be immediately viable.

I would prefer to implement a dynamic check for the lifetime of a given SP based on the current mass of the particle. However, given the time constraints of this project, and that this is a fairly small aspect of the overall implementation that could be added when required for general simulations, I chose to stick with this model instead.

4.4.3 The 'Supernova Time'

The last condition that I implemented is not a product of the physical parameters of the SP, but rather it is a consequence of the supernova evolution itself.

Supernova evolution takes time. Estimates for the lifetime of the Sedov phase put it at hundreds of thousands of years, §3.3. The time taken for a supernova to reach a particular radius for a given set of physical conditions can be described by:

$$t = 1.5\,\mathrm{kyr}\left(\frac{E}{10^{51}\,\mathrm{erg}}\right)^{-\frac{1}{2}}\left(\frac{n}{5\,\mathrm{cm}^{-3}}\right)^{\frac{1}{2}}\left(\frac{R_s}{5\,\mathrm{pc}}\right)^{\frac{5}{2}}. \tag{4.2}$$

Higher ambient densities outside of the supernova or examining larger radii can dramatically increase the amount of time required for the shock wave to expand to that size.

Since this implementation inserts a supernova at a particular point during its evolution, we need to consider the time it would have taken for the supernova to evolve to that point. In order to avoid introducing the effects of hundreds or thousands of years of evolution immediately, I created a condition called the *Supernova Time*. This is implemented as a SP property, allowing the value to be modified and tracked for each SP throughout the entire simulation rather than being generated each time it is required.

The Supernova Time (ST) of a given SP represents the earliest simulation time that the supernova solution for the SP can be introduced. It is defined as the sum of the creation time of the SP, the age requirement, and the evolution time associated with the solution. This final condition is therefore that the simulation time is greater than the ST for the SP.

However, the calculation of the evolution time depends on the ambient density in the region surrounding the SP, see (4.2). This can only be calculated dynamically as the simulation is running, provided that the previous two conditions are also met. To account for this I zero-initialise ST for each SP, thus trivially fulfilling the third condition. The SP will not be triggered by the supernova module until the other two conditions are met, at which point the module enters a loop to gather information about the simulation.

This loop iterates through all of the cells within the simulation, finding all cells within the provided supernova radius of each SP fulfilling the three conditions. During this process the total mass and volume is recorded for each supernova region. From these two values we can calculate the ambient density in each region.

Next the module checks if the Supernova time for the SP is still zero — i.e. if the ST has not been set yet — and if so it will determine the corresponding value using (4.2), given the calculated ambient density.

4.5 Interpolating into the Free Expansion Phase

As the Sedov phase is a particular phase of the evolution of a supernova one cannot assume that a supernova at a given radius can always be described by the Sedov solution. Ideally, the solution to this problem is dynamically choose the supernova radius so that that the supernova is always in the Sedov phase.

This radius can be chosen to obey either one of two conditions that signal the start of the Sedov phase, and consequently the end of the free expansion phase. These conditions are:

- The refractory shock from the expanding supernova reaches the centre of the supernova region [Hoefner 2010], and

- The expanding shock of the supernova has picked up as much mass as the supernova originally ejected [Simpson et al. 2015].

While both can provide estimation for the point at which the free expansion phase becomes the Sedov phase, it is far easier to estimate the latter. As such, this is the condition that I employ to signal the phase change in my code.

However, the information necessary to estimate this radius is not always easily accessible. Previous supernova implementations in other code-bases have solved this issue at the cost of computational complexity by expanding the radius that they want to use out until the amount of mass inside satisfies the condition[Bubel 2016]. While this is a feasible approach in FLASH, it would vastly increase the computational complexity of the code compared to having a fixed radius. Additionally, I want the user to be able to set the supernova radius to a particular value that they could base on the resolution of the simulation. This has the added benefit of allowing the user to ensure some basic level of resolution on the sphericity of the input supernova solution.

The solution to this problem is therefore to allow the user to set a supernova radius, and then modify the model that is being inserted for the supernova depending on the regime that the supernova will fit into based on the conditions within that radius. Due to the scales that the supernova module is intended for I can safely rule out having a supernova radius that is in the Snowplow phase. Therefore, I only need consider the Sedov phase and the Free Expansion phase for this module.

Little information is actually known about the Free Expansion phase of supernova evolution, partially due to its extremely short lifetime. A supernova in typical ISM densities will only exist in the Free Expansion phase for less than 300 years [Mushotzky 2010]. In order to model the free expansion phase I have made two key assumptions:

1. During the free expansion phase the supernova expands freely, i.e. the rate at which the shock is expanding is a constant,

2. At the instant the supernova occurs, all energy associated with that supernova is thermal energy.

The former allows me to easily determine the shock speed of the free expansion phase by simply calculating the shock speed at the Sedov Radius — the radius at which the Sedov phase begins — as this will also be the free expansion speed. The latter provided me with a condition that any model I derived had to fulfil.

$$\rho(\eta) = \rho_0 \tag{4.3}$$

$$v(\eta) = \frac{\eta}{\eta_s} v_s \tag{4.4}$$

$$P(\eta) = P_0 \tag{4.5}$$

The model that I chose was simple; distribute all physical quantities uniformly throughout the supernova radius, and insert a linear velocity profile that goes from zero at the centre of the supernova to the Sedov velocity at the provided radius, The basic implementation is found in . The motivation for the model was found in previous supernova implementations that found uniform distributions will evolve in such a way as to approach the analytical Sedov solution over time[Simpson et al. 2015; Bubel 2016].

4.5.0.1 Implementation of the Free Expansion Phase

The implementation of the free expansion phase into the supernova module occurs after the ambient density around the given SP has been calculated. Using this value and amount of mass that the supernova will inject, the value for the Sedov radius can be calculated using:

$$r_{sedov} = \left(\frac{3M_{inj}}{4\pi\rho_0} \right)^{\frac{1}{3}}. \tag{4.6}$$

This can then be compared to the user-supplied supernova radius to determine if the inserted supernova will be in the Sedov or Free Expansion regime. Based on the result of this comparison, the *kinetic fraction* for the SP's supernova solution can be determined. As shown in §4.10.2.2 the Sedov solution has 28% of its total energy as kinetic energy, with the remaining 72% in thermal energy. However, the exact distribution in the free expansion phase will vary depending on the radius chosen, and hence how close we are to the Sedov regime. Due to the fact that the free expansion profiles are invariant of the radius that we select, the total amount of kinetic energy contained within the free expansion model at a given radius only depends linearly on the radius, i.e.

$$f_k = 0.28 \times \frac{r}{r_{sedov}}. \tag{4.7}$$

The kinetic fraction, f_k, is then used to determine the amount of energy to put into the kinetic and thermal regimes within the free expansion phase based on the total supernova energy.

4.6 Conservation Methods

The most important requirement of a numerical simulation is arguably to enforce conservation. Conservation of energy and momentum are fundamental, universal laws that govern all interactions. Hydrodynamic simulations that fail to either account for these laws, or violate them, would yield non-physical results.

Conservation occurs in two distinct stages in the supernova module. The first stage involves measuring all of the quantities that the code will be introducing to the simulation. The reason that I cannot just simply assume a constant amount for any of the quantities to be introduced is that they depend directly on the local values, and will hence vary. Each of the quantities to be introduced are first measured within the each cell within the supernova radius of a SP that is undergoing the supernova process. These total amount of each quantity is then recorded.

At this point we know the three quantities required for conservation: the initial amount of each quantity within the supernova radius, the amount that the solution will introduce based on the current conditions, and the analytical amounts that we should be introducing. We can therefore calculate conservation parameters for each of the quantities that we want to track. These parameters take the form of scaling factors that we can use to modify the values that we are inserting to the solution so that the module has a net conservation.

For mass, thermal, and kinetic energy this is a simple calculation. Take the initial value X_i, add the analytical amount that we want to introduce X_{inj}, and divide by the amount the solution is actually introducing X'. Because FLASH deals with the specific internal energy — i.e. the total amount of thermal energy in the cell depends on the mass — and the kinetic energy clearly depends on the mass, both of these scaling factors will also have to account for the mass scaling factor.

$$M_{scale} = \frac{M_i + M_{inj}}{M'} \tag{4.8}$$

$$K_{scale} = \left(\frac{K_i + K_{inj}}{K' M_{scale}}\right)^{\frac{1}{2}} \tag{4.9}$$

$$U_{scale} = \frac{U_i + U_{inj}}{U' M_{scale}} \tag{4.10}$$

$$\tag{4.11}$$

Note that the kinetic scaling factor, K_{scale} has a square root. This is because we can either scale the mass, or the velocity to change the kinetic energy. However, we already have a conservation constraint on the mass so we need to modify the velocity. As kinetic energy is proportional to the square of the velocity then our scaling factor needs to be the square root of the required scaling when we apply it.

Conserving momentum, however, requires a different approach. We assume isotropy for the inserted supernova, so the code should not be adding any net momentum to the simulation. The method for calculating the momentum conservation parameter is therefore to first determine the momentum change in each cardinal direction caused by the introduction of the solution. Using this value we can then determine the centre of mass velocity, v_{com}, corresponding to this change and then subtract it from each of the inserted velocities.

$$p_f = p' M_{scale} K_{scale} \tag{4.12}$$

$$v_{com} = \frac{p_f - p_i}{M' M_{scale}} \tag{4.13}$$

Once all of the conservation parameters have been calculated, the solution can be inserted with the necessary modifications to ensure conservation.

4.7 Tests of the Supernova Implementation

The majority of the tests that I ran to test the implementation are one of two types of tests: a shell analysis, and a profile analysis.

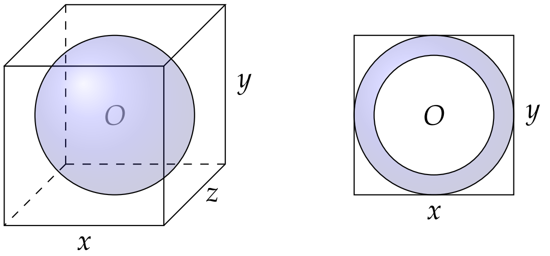

Figure 4.2: A diagram depicting a shell analysis. The left image shows the region being measured in 3 dimensions, while the right image is a slice of the measurement region on the x-y plane.

The shell analysis consists of examining each of the conserved quantities (mass, momentum, and energy) as well as the maximal radial velocity within a shell of some finite width that is pressed against the outside of the simulation box, see Figure 4.2. I use this test to examine the sensitivity of the inserted solution to the initial conditions, comparing the evolution of different initial radii.

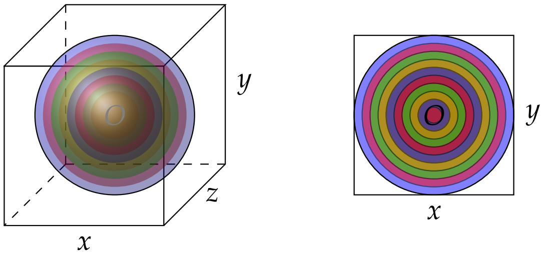

Figure 4.3: A diagram depicting the measurement regions used in the profile analysis. The left image shows the concentric shells within a 3 dimensional box, while the right image shows a slice of the measurement region on the x-y plane.

The second type of test is a profile analysis. This is similar in style to the shell analysis, but it employs a series of concentric shells from the centre of the simulation box to the edge of the box. Within each of these shells I determine the mean density, radial velocity, pressure, and thermal energy. This allows me to examine the development of the expanding shock, as well as provide an opportunity to compare the various profiles to the analytical Sedov profiles.

4.8 Using the Isothermal Equation of State

My original implementation of the supernova module used the **Bouchut3_isothermal** solver. As this solver uses the isothermal equation of state, (4.14), the internal energy of the gas (the temperature) remains constant throughout the simulation. As discussed in §2.3.4 the Bouchut3 solvers solve the equation of state during each time-step — overwriting the simulation's pressure variable to ensure the equation of state holds.

$$P = \rho c_s^2 = \rho \frac{k_B T}{\overline{m}} \tag{4.14}$$

This means that my original implementation did not include the pressure profile, instead choosing to focus solely on the kinetic energy portion of the Sedov solution. I also scaled the velocity profiles such that the inserted energy is equal to the assumed supernova energy of $E_{SN} = 10^{51}$ erg, see §2.1.2.

4.8.1 Initial Testing

One of the first things to be test is ensuring that the solution evolves in the same way regardless of the radius of the inserted supernova. In order to do this I need to determine the number of cells required for the supernova radius to adequately resolve the sphericity of the supernova solution.

For the purposes of these tests, and for all later tests unless otherwise specified, I employ a resolution of 64^3 cells within the simulation box. The box itself was a cube with side length 4.15 pc with a uniform density of 10^4 cm^{-3}. I introduce the supernovae at the centre of the cube with initial radii corresponding 4, 8 and 16 cells, the physical sizes of these radii is given in Table 4.1.

Radius (cells)	Radius (pc)
4	0.26
8	0.52
16	1.04

Table 4.1: The simulation and physical sizes of the supernova radii examined during the radial test.

Initial tests were conducted visually, examining the effect of the different radii on the evolution of the shock wave. One result that became immediately obvious was that mapping the spherical supernova solution onto the Cartesian grid of FLASH produced significant instabilities in the expansion of the shock wave, this is discussed further in §4.8.2.1. Due to the method of insertion adjacent cells on the outer perimeter of the supernova can have a significant difference in both their masses and their velocities. The presence of these discrepancies leads to highly asymmetric evolution of the supernova solution as seen in Figure 4.4.

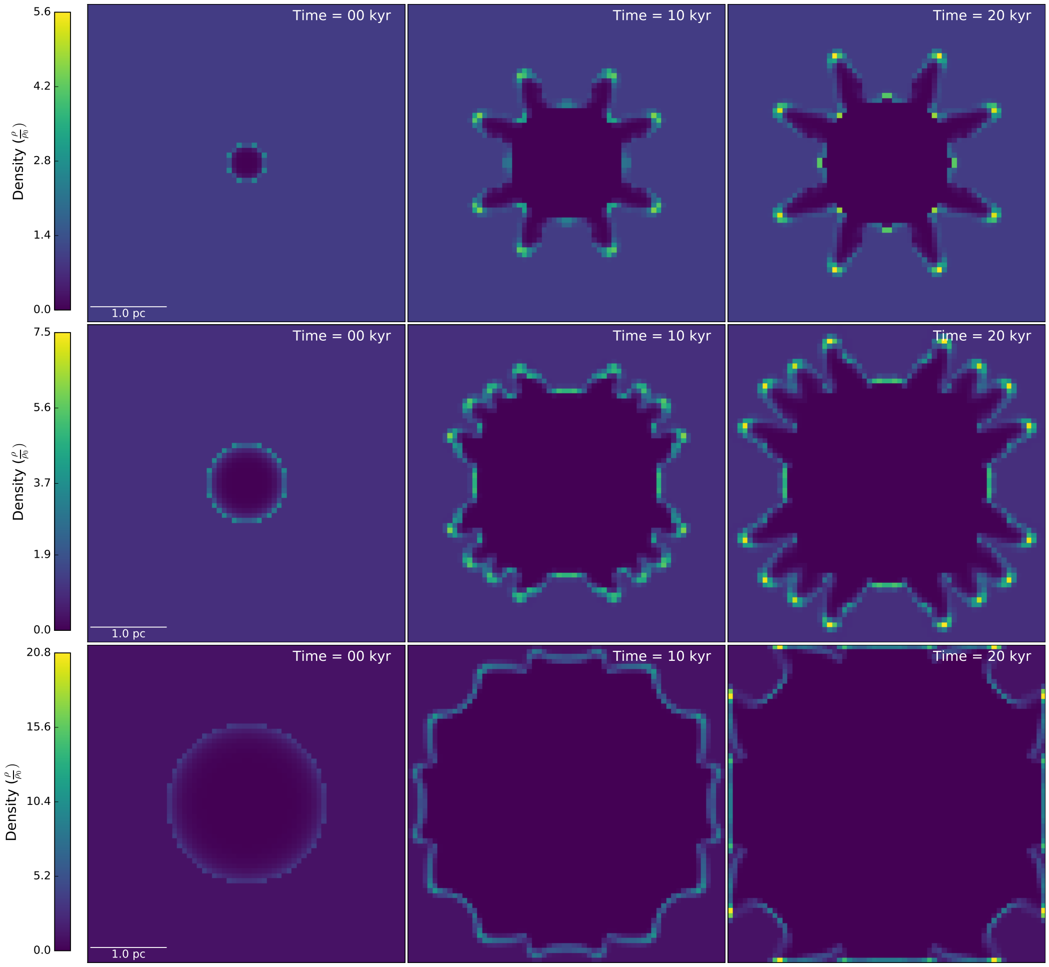

Figure 4.4: A slice along the x-y plane of the simulation box for different initial radii at the same resolution level. Rows from top to bottom correspond to initial radii of 4, 8, and 16 cells. The mean density, ρ_0, in each simulation is 10^4 cm $^{-3}$.

These results show that as the simulation progresses the expanding shock front becomes unstable in each test. However, the rate at which the shock becomes unstable depends on the initial radius. Smaller initial radii create a solution that becomes unstable faster, and conversely, larger initial radii become unstable slower.

4.8.2 Introducing a Smoothing Function

In order to limit the resulting instabilities I decided to include a smoothing function that can be applied to the Sedov profiles. This lowers the impact of the instabilities resulting from the insert of the supernova.

4.8.2.1 The Mathematical Basis for Smoothing

One of the major difficulties in implementing the supernova solution is the issue of mapping a sphere onto a discrete Cartesian grid. Increasing the number of cells in the sphere's radius will decrease the discrepancies between the mapping and the ideal sphere. However, in practice increasing the resolution of a sphere adds additional computational cost to inserting the sphere due to the increased number of cells.

Due to this relationship there is a trade-off between the accuracy of the inserted solution when compared to the analytical solution, and the cost required to insert the solution. Smaller radii are faster to insert, and also modify less of the simulation itself, but produce greater levels of instability in the inserted solution. These instabilities are the result of the method that FLASH uses to determine the position of a cell within the grid. The position of a given cell is defined as the position of its centre, and as such the distance between any position within the grid and a given cell is the distance between that point and the cell's centre. As the values for the Sedov solution are radially dependent, the value that the solution assigns to a given cell relies only on the position of that cell relative to the SP. Additionally, as cells represent the finest level of resolution in the simulation, any value that is calculated is applied to the entire cell.

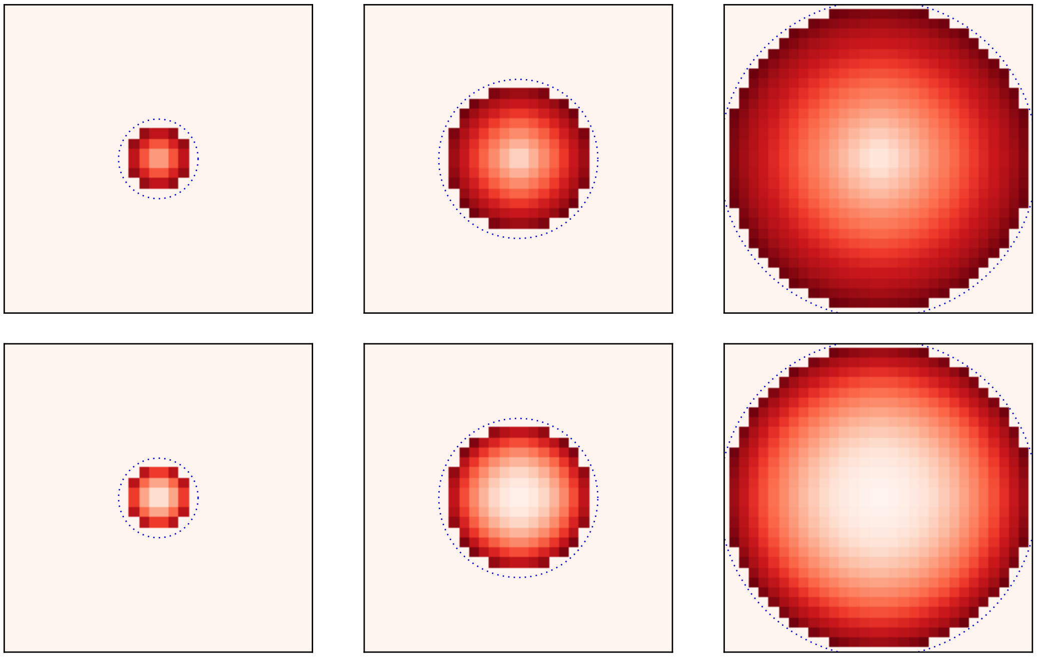

Figure 4.5: A series of images depicting the issue of mapping a circle onto a 2D discretised grid. From left to right the blue-dotted line represents a radius of 4, 8, and 16 cells from the centre of the image. The value of each pixel within this radius is given by the ratio (top) or the ratio squared (bottom) of the cells distance from the centre of the image to the blue line's distance. The colormap used has been normalised across all images to show consistent values.

Issues begin to arise when one considers the cells on the extremities of the supernova solution. Because of the nature of the grid situations can arise in which two adjacent cells can have one cell just outside and one just inside of the supernova radius. Hence one cell will receive the maximum values for the Sedov solution, while its neighbour will not be changed. This produces a discrepancy in the inserted solution that in turn causes instability in the evolution of the supernova.

An example of this can be seen in Figure 4.5 where the value of the each pixel within the blue line, in this case an analogue to the supernova radius, is dependent on the distance the pixel is from the centre of the image. The 4 cell images show significant differences in the colour of the outer layer of pixels, with the variance of the colour decreasing with the larger radii. The second row shows the same radii, but with the color value dependent quadratically on the radius. This is to demonstrate the effects of a more rapidly increasing function, such as the Sedov density profile, see Figure 3.2. Again, the differences between adjacent cells on the outer layer for the 4 and 8 cell examples are quite apparent.

The method I employed to combat this consists of introducing a smoothing function. This smoothing function would limit the magnitude of the discontinuities between adjacent cells on the supernova boundary, and therefore reduce the resulting instabilities. I had two requirements that the function had to fulfil:

1. It preserves the shape of the profiles within the outer few cells of the supernova radius.

2. It needs to smoothly decrease towards the outer limits of the supernova radius.

The combination of these requirements would significantly lessen the observed discontinuities of the injected supernova solution, while preserving the internal structure. The function that I selected is:

$$f(x|m,s) = \frac{e^{ms}}{e^{ms}+e^{sx}} = \begin{cases} 1 & x \ll m \\ 0.5 & x = m \\ 0 & x \gg m \end{cases} \tag{4.15}$$

For the purposes of this module the value of m was set to the edge of the shock, i.e. $m = \eta_s$. The parameter s controls the 'sharpness' of the transition from 1 to 0. For $s \to \infty$ the smoothing function recovers the Heaviside function, and would hence leave the solutions unchanged — for the simulations that I performed I set $s = 40$. An example of the profile of the smoothing function can be found in Figure 4.6. An example of the effect that the smoothing function has on reducing the level of variance on the edges of the inserted solution can be seen in Figure 4.7. The homogenising effect of the smoothing function can be clearly seen on the 8 and 16 cell examples reducing the discontinuities seen in the non-smoothed examples.

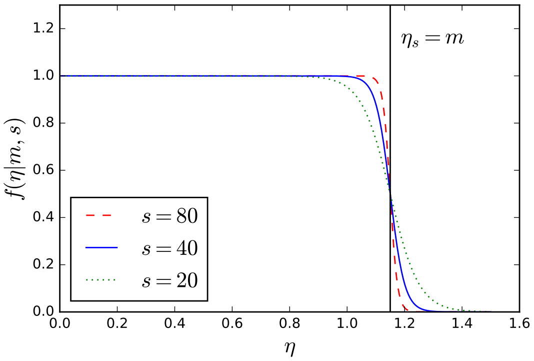

Figure 4.6: A plot of the smoothing function described by Eq. (4.15) for $m = \eta_s = 1.15$, and a variety of sharpness values.

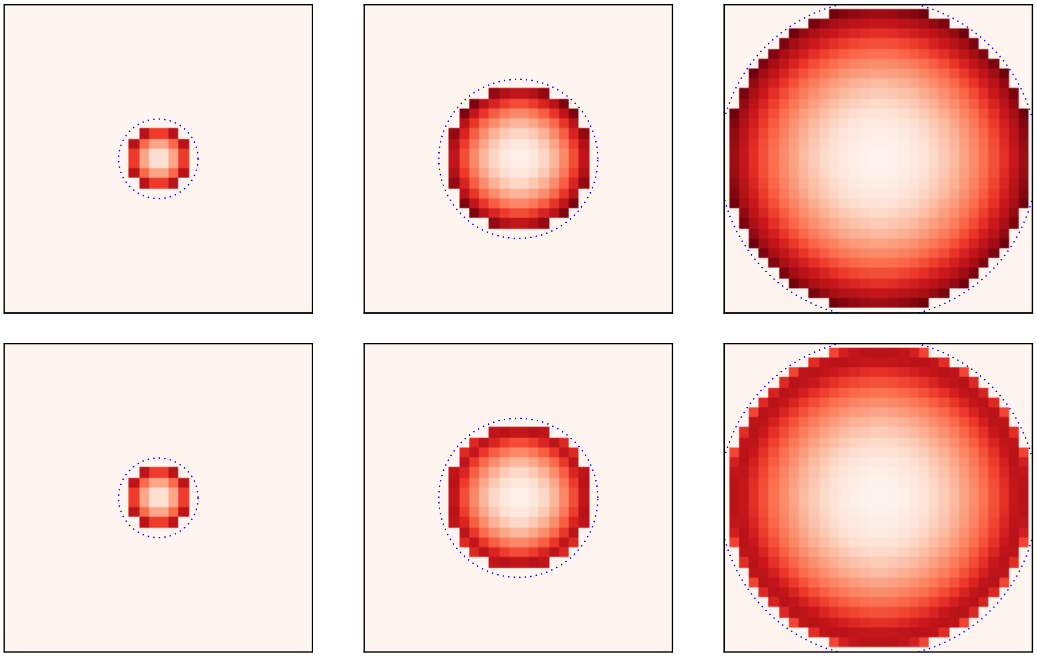

Figure 4.7: A series of images showing the effect of the smoothing function on a map of a circle to a 2D grid. From left to right the images correspond to radii of 4, 8, and 16 cells respectively. The value in each cell depends quadratically on the ratio of the distance the cell is from the centre of the image to the radius of the blue line, $f(r) = \left(\frac{r}{R}\right)^2$. The sharpness of the smoothing function used was $s = 40$, with m positioned at the blue line.

4.8.2.2 Implementation Details

The smoothing is implemented as the second *model* in the Supernova module. It can be activated by setting **sink_supernova_model** to 2 in the **flash.par** file. When this model is activated the smoothing function is be applied to the Sedov profiles immediately after their generation.

The required sharpness of the smoothing function depends completely on the number of cells that need to be modified, as well as the overall size of the inserted solution. Typically, only the two outer layers of the supernova solution would need to be modified to reduce the discontinuities, however the proportion that those cells are to the total number of cells in the supernova radius needs to be considered. As such, the value of s can be modified using the **sink_supernova_sharpness** parameter.

4.8.2.3 Examining the Results

With the smoothing function implemented, I repeat the previous simulation to gauge if the smoothing function reduces the instabilities.

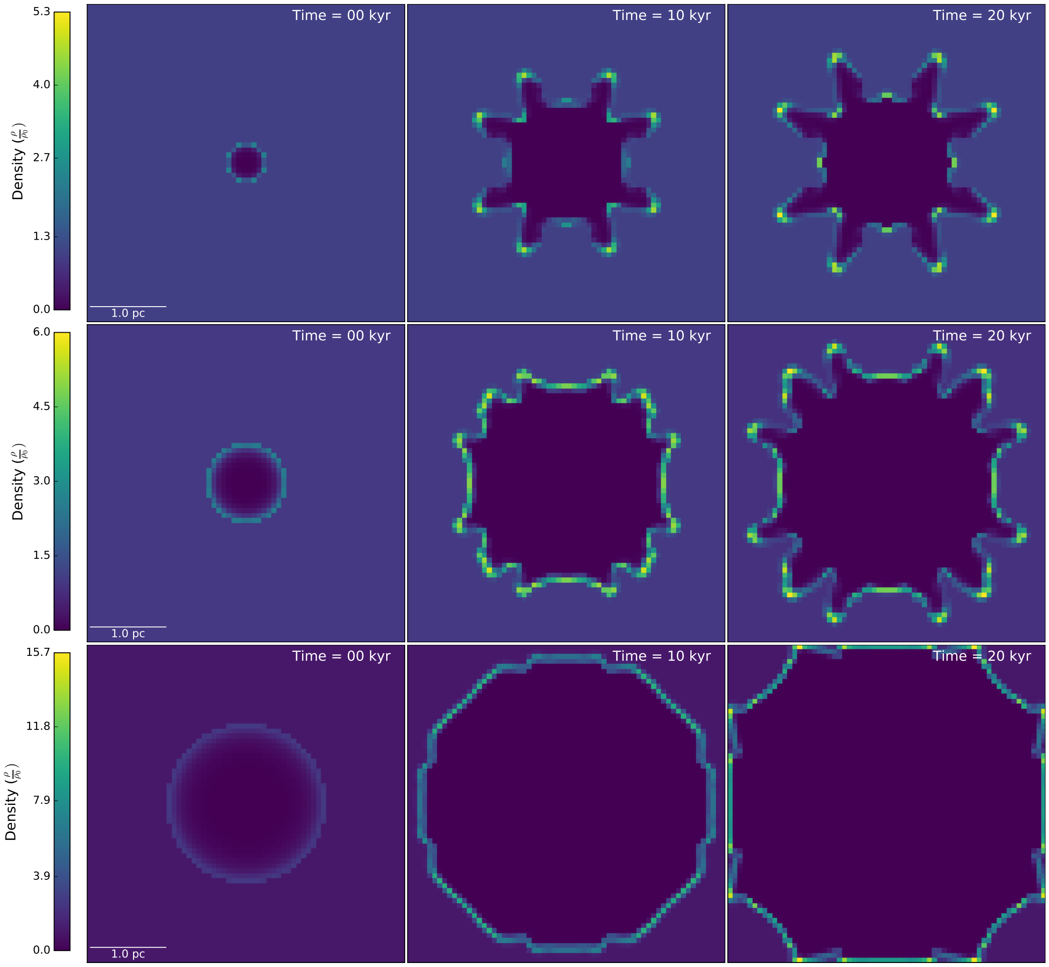

Figure 4.8: A slice along the x-y plane of the simulation box for different initial radii at the same resolution level. Rows from top to bottom correspond to initial radii of 4, 8, and 16 cells. The mean density, ρ_0, in each simulation is 10^4 cm^{-3}.

Comparing the results in Figure 4.8 to the un-smoothed tests in Figure 4.4 it is clear that the smoothing function does generate marginal improvements to the sphericity of the expanding shock. However these improvements are only noticeable in the latter two tests: 8 and 16 cells per supernova radius. Based on these results I decided to maintain the smoothing function in the code as minor improvements to the stability are still improvements.

Additionally, these results give an insight into the minimum resolution of the supernova sphere required to accurately reproduce the evolution of the analytical solution in an isothermal gas. I find that at least 8 cells is required for the supernova radius in order to ensure smooth expansion of the shock. However, as this assessment was based on a visual examination it is also important to quantifiably demonstrate this with an experiment.

4.8.3 Radial Testing of the Supernova Implementation

Here I replicate the previous test to examine the radial dependence of the supernova implementation, this time using the smoothing function. This involves a shell analysis, as described in §4.7. These simulations were run over a period of 30 kyr of simulation time to ensure the expanding supernova blast wave had time to propagate to the edges of the computational domain.

The shell used for the analysis was 0.52 pc thick and positioned at the extremities of the box. Within the shell I calculate the total amount of mass, the radial momentum, the kinetic energy, and the maximum radial velocity throughout the duration of the simulation. The results of this test can be seen in Figure 4.9.

It is clear from the analysis that the solution does not converge for different initial radii when using the isothermal equation of state. Furthermore, we can see that the majority of the kinetic energy has dissipated by the time that the smaller two radii (4 and 8 cells) reach the shell boundary.

4.9 Using the Polytropic Equation of State

Based on the poor performance of the Supernova implementation using the isothermal equation of state, I try a polytropic equation of state next. This was a case of changing solvers to the **Bouchut3_polytropic** solver. The polytropic equation of state introduces a polytropic constant of Γ to the simulation, effectively stiffening the gas and reducing the rate of energy loss by the supernova shock. The value of Γ used was $\frac{5}{3}$.

$$P \propto \rho^{\Gamma} \tag{4.16}$$

Again, I repeat the same set of tests to examine the effects of the new changes to the supernova implementation. Ideally, the stiffer gas should help reduce the instabilities and provide a higher level of convergence in later tests. The results of this set of tests can be found in Figure 4.10.

The effect of stiffening the gas is already evident when examining the stability of the expanding shock in the polytropic gas (Figure 4.10), compared to the isothermal tests in Figure 4.8. We can see that the 8 cell test using the polytropic equation of state

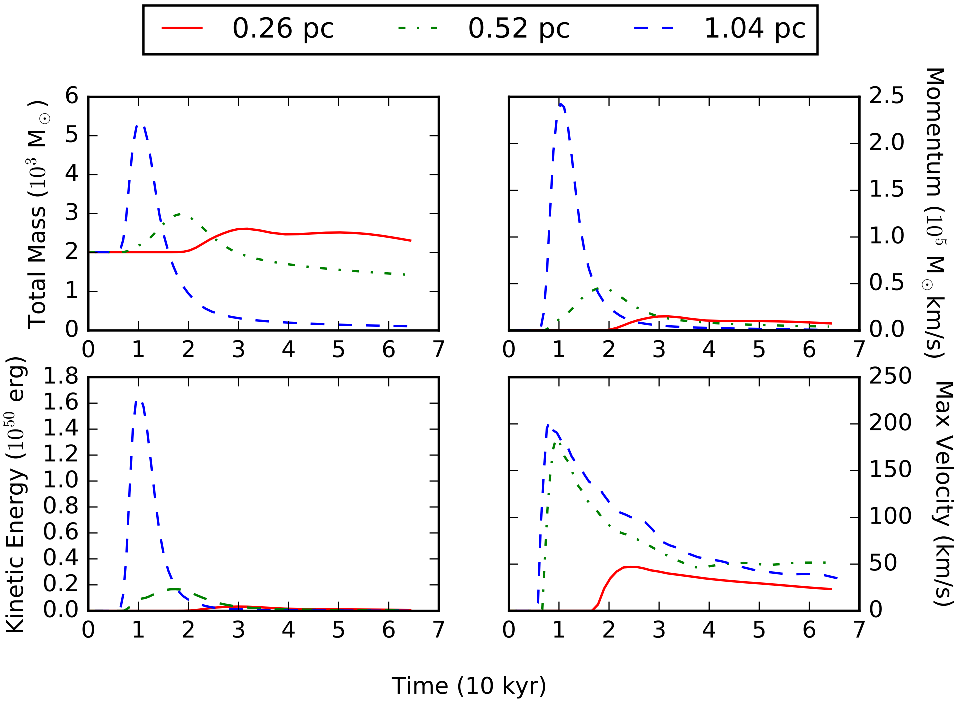

Figure 4.9: The results of a shell analysis for a test using the isothermal hydrodynamic solver. The plot shows the amount of each quantity within a shell placed at the edge of the simulation box over the course of a simulation. The different lines represent the different initial supernova radii — corresponding to initial radii of 4, 8 and 16 cells at highest resolution — with values given by the legend. The box width is 4.15 pc, with a uniform density of 10^4 cm^{-3}.

maintains the spherical shock far better than the isothermal equation of state over the first 10 kyr of the simulation. After 20 kyr there are significantly fewer deviations from a spherical shockfront and the deviations that do exist are less pronounced than previously.

4.9.1 Testing for Radial Dependence

After seeing some positive results from the stability test I repeat the radial dependence test to determine if the polytropic equation of state would reduce the lack of convergence that I had observed with the isothermal equation of state. The results of this test can be found in Figure 4.11.

Overall the results of this test were not much better than what we saw with the isothermal equation of state. There is still a high level of variation in the values measured by the shell. As before, this appears to indicate that the supernova solution is losing the majority (>95%) of its kinetic energy by the time the 0.26 and 0.52 pc solutions reach the shell. By comparison the supernova shock with an initial radius of 1.04 pc only loses around 80% of its energy by the time that it reaches the shell.

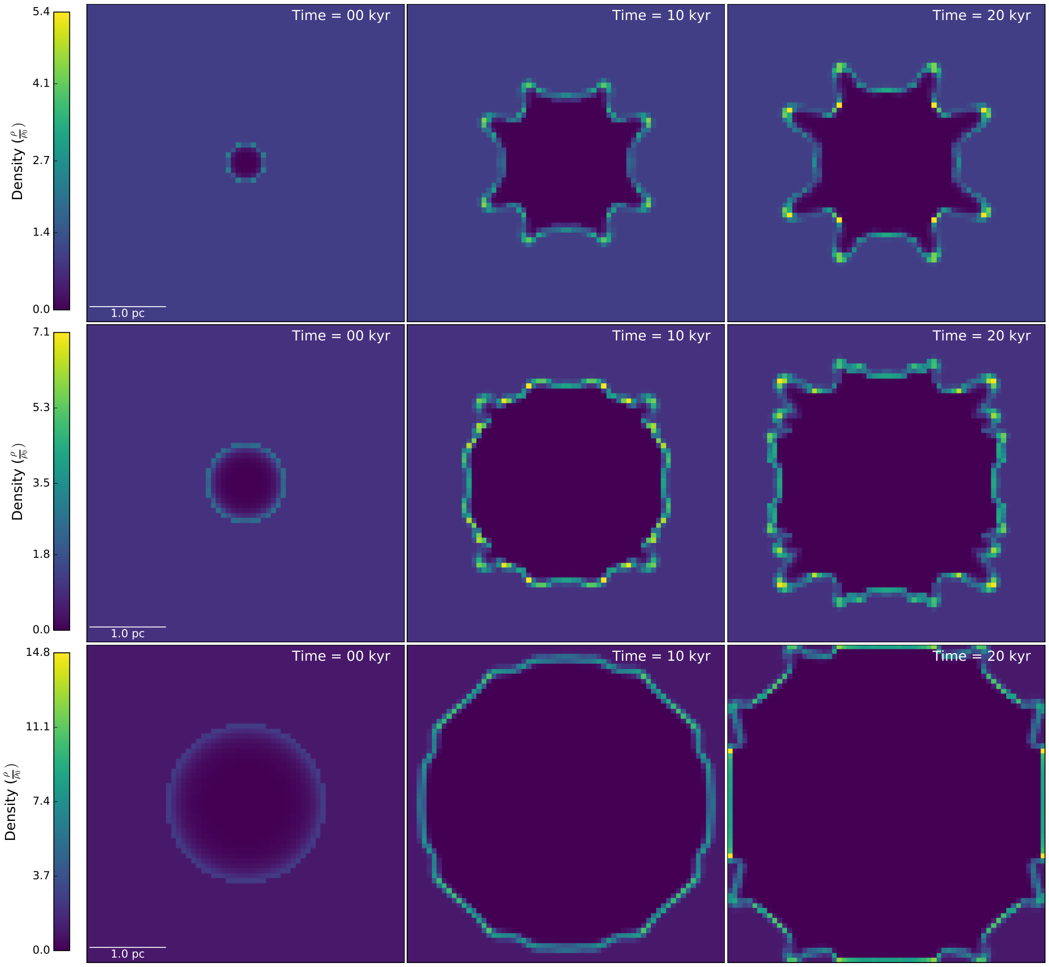

Figure 4.10: A slice along the x-y plane of the simulation box for different initial radii at the same resolution level. Rows from top to bottom correspond to initial radii of 4, 8, and 16 cells respectively — the physical size of these radii can be found in Table 4.1. The mean density, ρ_0, in each simulation is 10^4 cm^{-3}.

4.9.2 Exploring the Effects of Resolution Levels

Despite the poor results from the radial testing, I also perform a resolution test using the polytropic equation of state to determine if the solution was at least consistent for different resolutions. An ideal simulation model should not have its accuracy be dependent on the resolution of the simulation so this can help us determine if the module has any significant dependence on the simulation parameters.

The conditions for the test are identical to the radial dependence test, but with the radius of the inserted supernovae fixed to a physical size of 0.52 pc. I run a set of 3 tests, beginning with a resolution of 64^3 cells, and increasing the resolution by a factor of 2 in each cardinal direction until reaching a final resolution of 256^3 cells. I then perform a shell analysis on the output of each test, the results of which can be seen in Figure 4.12.

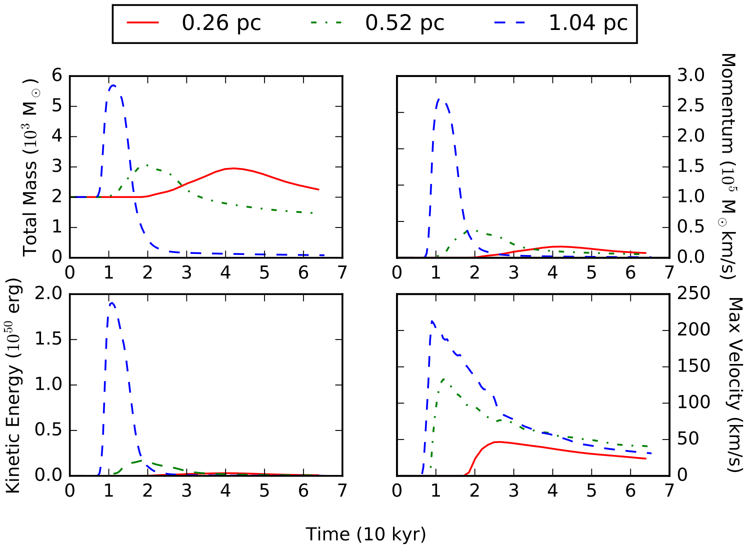

Figure 4.11: The results of a shell analysis for a radial dependence test performed under the polytropic equation of state. The plot depicts the amount of each quantity within a shell placed at the edge of the simulation box over the course of the simulation. The different lines represent the different initial radii. The physical values are given in the legend and correspond to a resolution of 4, 8, and 16 cells respectively. The box width is 4.15 pc, with a shell width of 0.52 pc.

These results are neither good nor bad. The supernova implementation doesn't seem to have a significant dependence on the resolution used in the simulation which is promising. However, the progression of the resolution levels from right to left in order of increasing resolution level is an interesting result that should be noted. The solutions do not appear to converge initially, however the momentum and kinetic energy values do tend towards the same values.

4.10 Using the Ideal Equation of State

Having determined that the polytropic equation of state was not producing a coherent Sedov blast wave I now begin using the Bouchut3 solver using the ideal equation of state shown in (4.17), where ε is the specific internal energy of the gas, and γ is the adiabatic gas constant. This also serves to combat the observed energy losses that were still present with the polytropic equation of state as well as the previous tests with the isothermal equation of state.

$$P = \rho\varepsilon(\gamma - 1). \tag{4.17}$$

My initial tests produce shocks that become decoherent far more quickly than they should under the analytical Sedov solution without cooling. Given that this was occurring under the ideal equation of state, it brought into question whether or not the

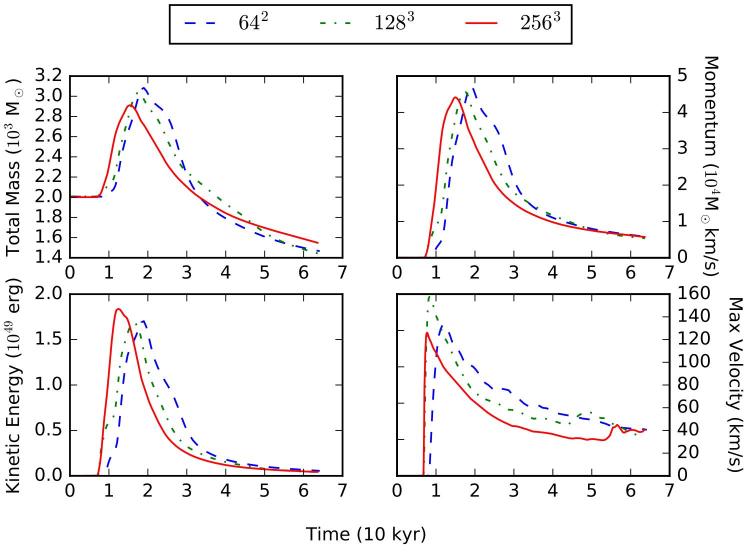

Figure 4.12: The results of the resolution test performed under the polytropic equation of state. The plot depicts each quantity within a shell placed at the edge of the simulation box over the course of the simulation length. The different lines correspond to different resolution levels. The box width is 4.15 pc, with a shell width of 0.52 pc, and a fixed supernova radius of 0.52 pc.

model I was implementing was correct, or if it *could* be correct outside of an idealised thought experiment. The analytical Sedov solution is self-similar and the Sedov phase of supernova evolution is a sustained phase, and the results of the tests until this point showed neither property.

Investigating this found that the density that I have used for the tests until this point is significantly higher than typical values for the interstellar medium — on the order of 10^4 cm^{-3}. Additionally, the length scales that I use for the simulations are much smaller than the typical supernova radius in the Sedov regime. Based on these observations I proceed to test the supernova implementation at significantly larger radii, with a lower mean density within the simulation.

4.10.1 Testing for Dependence on Physical Size

For this set of tests I use an gas density of 50 cm^{-3}, at a fixed resolution of 64^3 cells. To allow the inserted supernova to have the maximum amount of time to evolve during the simulation without self-interacting due to the periodic boundary conditions I also set the supernova radius to be 4 cells.

I begin the tests with a initial box size of 16.6 pc and then increase it by a factor of 2 with each subsequent test until reaching a final value of 132.8 pc wide[2]. This is effectively a resolution test, but rather than adjusting the resolution of the grid in the simulation, I am adjusting the physical size.

---

[2] At first glance these values may seem arbitrary, however this is due to FLASH using CGS units for its physical values. The original tests performed at a resolution 64^3 cells had a box size such that each cell was 0.1×10^{18} cm wide. This same box was then used as a template for this analysis, scaling the box

At the completion of each test I perform a profile analysis to examine the evolution of the density profile for the expanding supernova blast wave. This also allows me to directly compare the evolution of the implemented blast wave to the analytical Sedov solution under the same conditions.

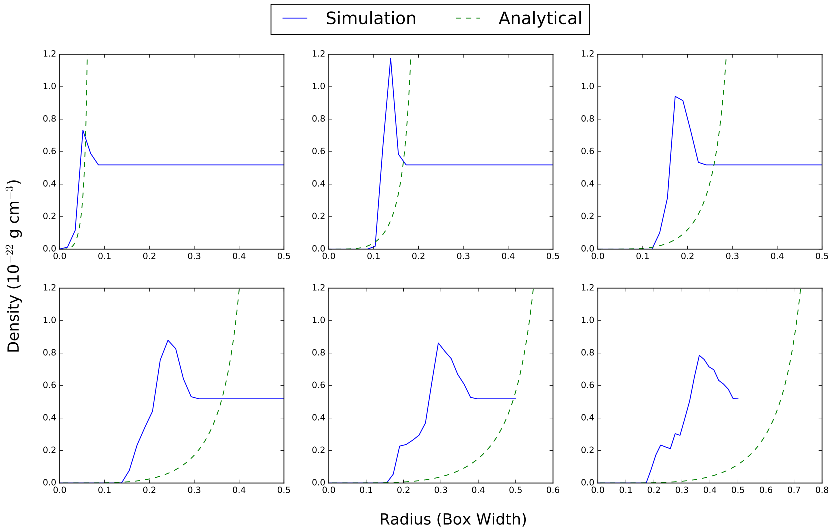

Figure 4.13: The self-similar solution observed during the size test. The images are a snapshot of the evolution of the shock-wave. They are in chronological order, left to right, top to bottom. The density profile is used as an indicator of the shock profile as it traces the overall shape of the shock.

In short, the results of these tests find that the inserted solution did not match the Sedov solution, nor did the ideal equation of state produce a truly coherent shock-wave at any point during the tests. However, a comparison of all of the results from the tests reveals that in each instance the shock-wave collapsed at the same relative point within the box during each simulation. This result is strongly compelling as it is a direct manifestation of the self-similar nature of the inserted profiles.

As the Sedov solution is independent of the time, or size of the supernova, introducing the supernova at a fixed size relative to the total width of the box the simulation ran identically in each instance. A comparison of the normalised profile from these tests with the Sedov solution can be found in Figure 4.13.

This also alleviates some of the concern over the very short period of stability that the solution was previously exhibiting. The time-scale of the solution is intrinsically linked to the size of the solution, therefore increasing the physical size of the supernova increases the amount of simulation time during which the shock remains coherent. Comparing the time of collapse for each of the different physical sizes measured in this tests can be found in Figure 4.14.

---

by a factor of 8 for the first test yielding a total width of 51.2×10^{18} cm = 16.6 pc.

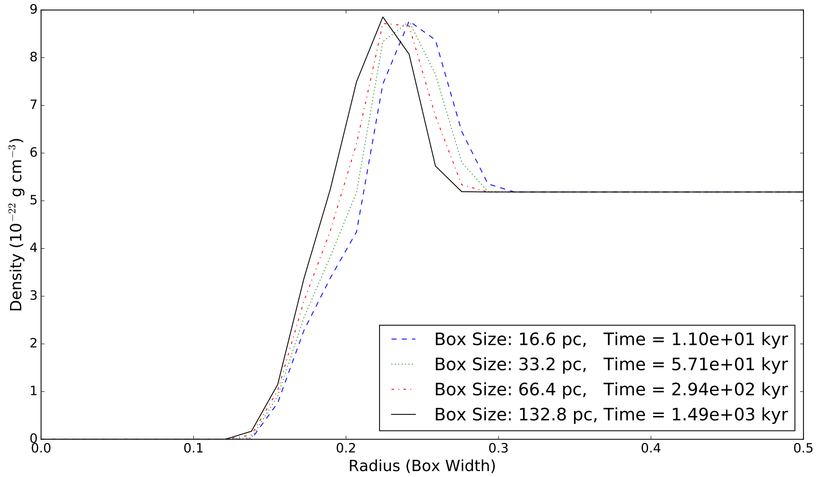

Figure 4.14: A comparison of the shock profile for different box sizes with the same initial ratio of the supernova radius to total box width.

4.10.2 Approaching the Analytical Solution

From Figure 4.13 it is apparent that the current implementation does not replicate the analytical Sedov solution. This is due to the fact that the implementation is still injecting energy solely into the kinetic regime, whereas the analytic solution inserts the majority of the injected energy into the thermal regime.

Until this point I have ignored the thermal energy component of the supernova as the previous equations of state did not allow for its inclusion. However, now that the solution is being tested under the ideal equation of state the internal energy can be accounted for correctly.

4.10.2.1 Extending the Sedov Solution to Include Internal Energy

Due to the method the Bouchut solvers use to ensure each cell adheres to the equation of state (see §2.3.4), we need to calculate an internal energy profile for the Sedov solution as the Bouchut3 solver overwrites the pressure in each cell at the end of each time-step.

The solution to this is to instead modify the specific internal energy such that the correct pressure will be inserted by the hydrodynamic solver. Solving the ideal gas equation for the specific internal energy yields

$$\varepsilon = \frac{P}{\rho(\gamma - 1)}. \tag{4.18}$$

From this equation we can calculate a specific internal energy profile that is consistent with the analytical Sedov solution by substituting in the pressure and density profiles given in (3.27) and (3.29). This produces:

$$\varepsilon(\eta) = \frac{2v_s^2}{(\gamma+1)^2}\left(\frac{\eta}{\eta_s}\right)^2 \frac{B(\eta)}{A(\eta)}, \tag{4.19}$$

wehre v_s is the shock speed, η is our dimensionless variable from the Sedov derivation, η_s is the position of the shock expressed as a dimenionless variable, and $A(\eta)$ and $B(\eta)$ are the Sedov density and pressure profiles respectively.

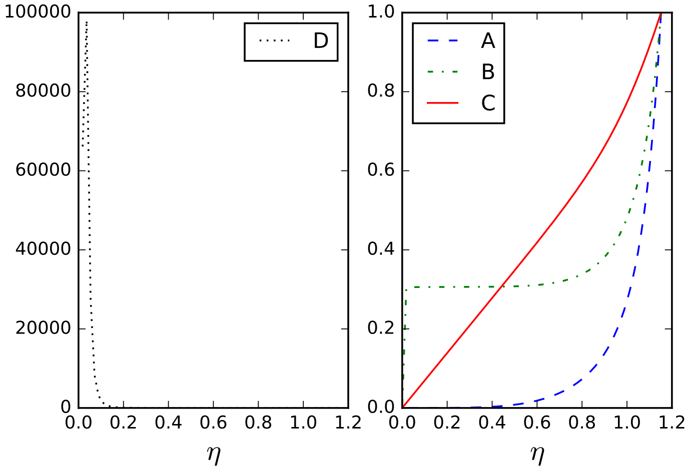

Figure 4.15: A plot comparing the original three Sedov profiles to the specific thermal energy profile. Note that this is using the derived values used in the simulations, and is presented in the raw form, without scaling by the adiabatic constant or shell speed, so that the right-hand image is equivalent to the image found in Figure 3.2

This is the final profile that I use for the supernova implementation. A plot showing the new internal energy profile next to the original Sedov profiles is found in Figure 4.15. We can see here that the internal energy profile is orders of magnitude larger than the other profiles, this is due to the inverse dependence on the density which tends to zero at the centre of the supernova. I will also note that the corresponding specific internal energy profile for the free expansion phase is uniform by the same reasoning as the rest of the profiles, see §4.5.

4.10.2.2 Determining the Energy Partition

As discussed in §3.2.5 the Sedov solution is defined as a conservational phase, maintaining a constant amount of energy throughout the evolution. This conservation principle is key in the derivation of (3.46) which describes the relationship between the Sedov profiles, A, B, and C and the total amount of injected energy E_{SN}. Examining this equation reveals that the integral is separable into two equations that detail the internal and kinetic energy distribution in the Sedov solution[3]:

$$E_{int} \propto \frac{32\pi}{25(\gamma^2-1)}\int_0^{\eta_s} B(\eta)\eta^4 d\eta, \quad E_{kin} \propto \frac{32\pi}{25(\gamma^2-1)}\int_0^{\eta_s} A(\eta)C(\eta)^2\eta^4 d\eta. \tag{4.20}$$

Substituting in the Sedov profiles yields 0.72 and 0.28 respectively, indicating that 72% of the injected energy goes into the thermal energy regime, and the remaining 28% of the energy is in the kinetic regime.

The supernova implementation now includes the internal energy profile, and as such is now a complete solution. To test this I run another test in a simulation box 66.4 pc wide, and compare the results of a profile analysis to the analytical solution. The comparison can be seen in Figure 4.16. We will note that the inserted blast wave and its evolution have a much lower density than the analyitical value. This is an artefact of introducing the profiles onto a discretised grid. As shown in Figure 4.1 the density profile becomes very steep as it approaches the supernova radius. As such, when inserting the solution onto a grid it is unlikely to get the edge and hence the maximum value. This is compounded by the fact that I want to chose an integer number of cells for the supernova radius, so the solution will always peak lower than the analytical solution.

The results of the comparison show that the inclusion of the internal energy brings the implementation to match the analytical solution exactly during evolution. The shape and the movement of the shock-front track the analytical solution over the whole range of the simulation accurately, and it also avoids the collapse of the shock-front that was present with the isothermal and polytropic solvers.

An interesting phenomenon in the top-middle image in Figure 4.16 is the bump in the density profile of the shock 1/3 of the way from the centre of the shock to the shockfront. This is actually a remnant of the refractory shock caused when the supernova shock first moved in the timestep after insertion. The image in question caught the shock during the passage back out to the shockfront.

This is actually a physical phenomenon that is theorised to occur within actual supernovae, and is the first of the two conditions that I discuss as potentially indicating the beginning of the Sedov regime in §4.5.

One notable result of introducing the internal energy is the significant reduction of the the instabilities in the shell that were present in tests with the other equations of state. This is especially evident for smaller initial radii; a comparison of the evolution of a 8 cell supernova under the isothermal, polytropic, and new complete solution can be seen in Figure 4.17. We can also see from this test that the addition of the forcing provided by the thermal energy, the resulting shock maintains a far higher speed than it did in the previous simulations.

---

[3] Note that while I am defining the values into the following set of equations to be proportional to an integral multiplied by a constant, I am not using $\propto$ in the traditional sense. The subtlety is that the integral portion is written in terms of our dimensionless coordinate system, η, in which energy is a constant set to 1. As such, this proportionality is equivalent to determining E_{int} and E_{kin} as a fraction of the total energy.

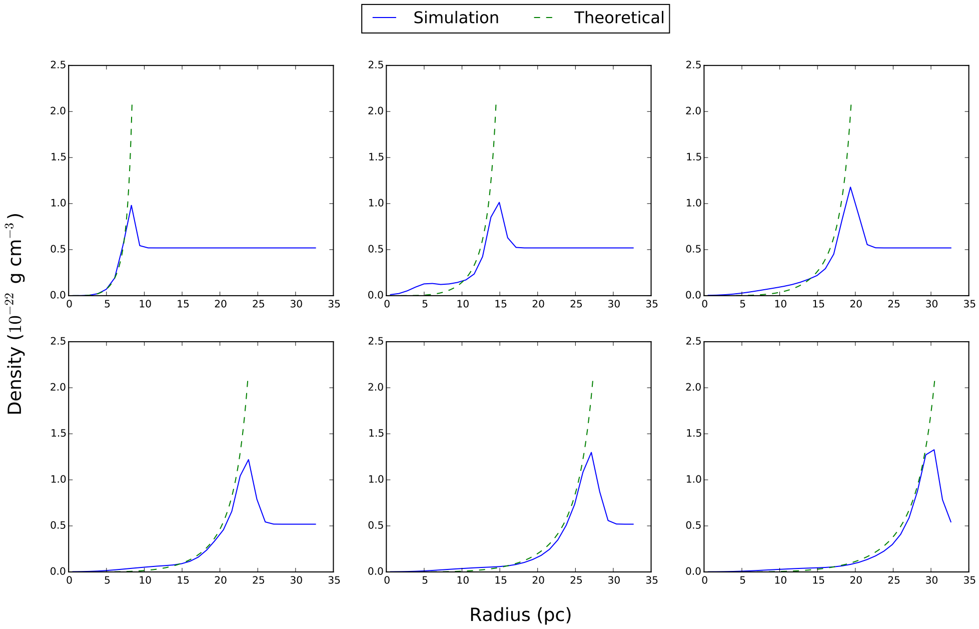

Figure 4.16: A comparison of the shock simulated using the ideal gas EOS against the the analytical Sedov solution. The simulation box has a uniform density of 50 cm^{-3}, and a total width of 66.4 pc with a resolution of 64^3 cells. The inserted supernova had a radius of 8.3 pc, the equivalent of 4 cells at the given resolution.

4.10.3 Modifying the Sedov Solution for Faster Simulations

While the supernova implementation now accurately reflects the idealised analytical solution, it is not ideal for a numerical simulation in the current form.

As discussed in §2.3.5 hydrodynamic solvers employ the CFL condition to ensure the stability of their solutions. Due to the high speeds of supernova shocks, and the very high temperatures in their cores the CFL condition can severely restrict the maximum allowable time-step. Specifically, the Bouchut3 MHD solver that I am using calculates a maximum time-step for the propagation of magnetic waves using the speed of sound, and the Alfven speed. The speed of sound within a gas is proportional to the temperature of that gas, so very high temperatures within the simulation could drastically reduce the allowable time-step.

This is the exact condition that occurs when introducing the complete Sedov solution. The temperatures in the centre of the supernova are many orders of magnitude larger than the typical temperatures in the ISM — high enough that they reduce the allowable time-step in simulations by up to 2 orders of magnitude more than the allowable time-step from the CFL condition using the shell speed.

This can be a significant limitation when running a simulation for the equivalent of millions of years, a two order of magnitude difference in the allowable time-steps can result in a two order of magnitude increase in the number of time-steps required for the same period. Given that the time taken to iterate the simulation during a time-step

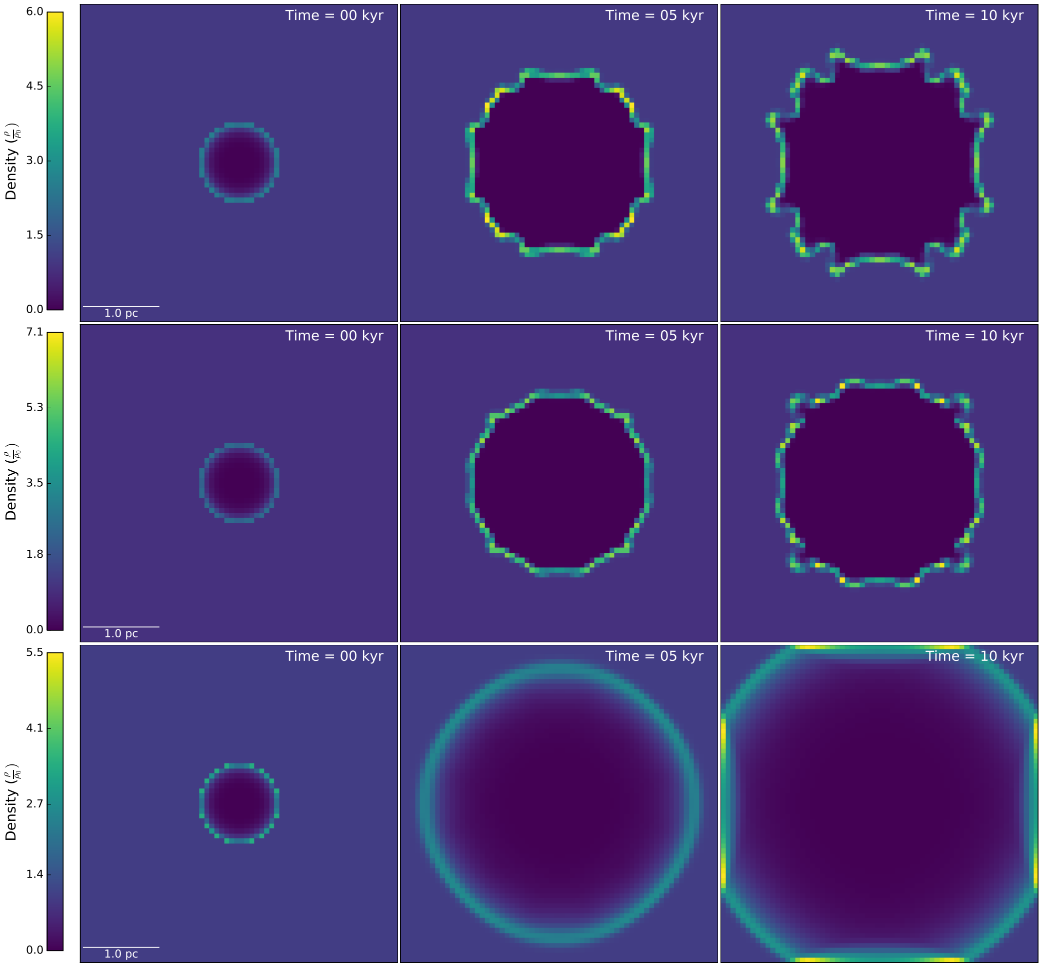

Figure 4.17: A slice along the x-y plane of the simulation box for the same initial conditions under different equations of state: isothermal (top), polytropic (middle), and ideal (bottom). The mean density, ρ_0, in each simulation is 10^4 cm^{-3}, and the initial radius used was 0.25 pc (8 cells).

is completely independent of the physical parameters of the simulation, it can also lead to a two order of magnitude increase in the wall clock time time required to run the simulation.

Due to this limitation there is an intrinsic trade-off that has to be considered during this point in the development of the supernova module: accuracy or optimality. Leaving the model in the current form would produce the most accurate results, replicating exactly the analytical Sedov solution that I set out to implement. However, this accuracy comes at a huge resource cost. While the module would be accurate, it would never be feasible for any large-scale or generalised simulation of a region of a galaxy — one of the main goals of this project.

My solution to this problem is as follows. I now include a boolean parameter **sink_supernova_analytical_profiles** that allows the user to select if they wanted to use the analytical Sedov profiles for their simulation or to use a modified set of profiles that reduces the time-requirement for the simulation.

The differences between the analytical and the optimised profiles are very minor. The velocity and the pressure profiles are identical in either case. The main differences are in the density and internal energy profiles which dominate the calculation of the maximum allowable time-step. This is due to the specific internal energy profile being inversely dependent on the density profile, see (4.19). The Sedov density profile, $A(\eta)$, becomes very small (~ 10^{-7}) towards the centre of the supernova, and in turn, the internal energy, and hence the temperature and speed of sound, become very large. This can be seen in Figure 4.15.

Ideally, the solution to this would be to provide a lower bound on the density profile. As this cannot be performed during the generation, I instead opt to add a small constant of 10^{-2} to $A(\eta)$ uniformly after generation. This has the effect of dominating towards the centre of the supernova solution when the density is 4 orders of magnitude smaller, while introducing an estimated 1% error at the forefront of the shock. The actual error will in fact be less than this as the amount of mass injected and the mass already within the supernova radius are enforced during the conservation steps through normalisation, and the majority of this mass is within the outer limits of the supernova profile anyway.

The final effect of the modification is that the maximum allowable time-step immediately following the injection of a supernova is increased by an order of magnitude. This in turn leads to an order of magnitude reduction on the time-taken for the simulation to 'recover' from the injection of the supernova to the ambient conditions.

4.11 Introducing Cooling to the Simulations

Finally, I implement cooling in the simulations. This is the final stage to making a realistic supernova implementation. As I discuss in §3.3 there are two conditions that signal the end of the Sedov regime of the supernova evolution. However, it is the energy conservation condition that dominates the calculation of the lifetime of the Sedov phase.

When applying this to a large-scale physical simulation, such as the exploration of supernova-driven turbulence I discuss in §5, it is not feasible to run without some kind of cooling, or ignoring the temperature and internal energy changes with an isothermal or polytropic equation of state. Under an ideal EOS, and without any cooling, the amount of inserted energy in either regime will be constant within the supernova radius at all times. While I have previously asserted this as one of the conditions of the Sedov solution, it should only be considered during the insertion of the supernova; ignoring the cooling during the evolution produces a shock that will continually expand regardless of the external conditions far beyond the determined end of the Sedov phase in §3.3.

To combat this I now include an implementation of the Sutherland-Dopita cooling function [Sutherland and Dopita 1993] into my version of FLASH4. The cooling function utilises the metallicity of the gas, as well as its density and temperature to determine the luminosity of the gas, and hence the rate of thermal energy loss. This cools the gas and produces a realistic lifetime for the Sedov phase of supernova evolution. Currently my simulations do not track the the presence of heavy elements, so I assume solar metallicity values in all simulations.

My final test during the development is a comparison of the evolution of the polytropic and ideal supernova implementation with and without cooling. This comparison can be seen in Figure 4.18. From this we can see that the polytropic and the cooled ideal equation of state test develop at the same rate, however the cooled test develops far fewer instabilities over the course of the evolution. It is worth noting that the polytropic test is using the smoothing function from §4.8.2. This confirms our conjecture that the inclusion of the internal energy is necessary to ensure stable evolution in the resulting blast-wave.

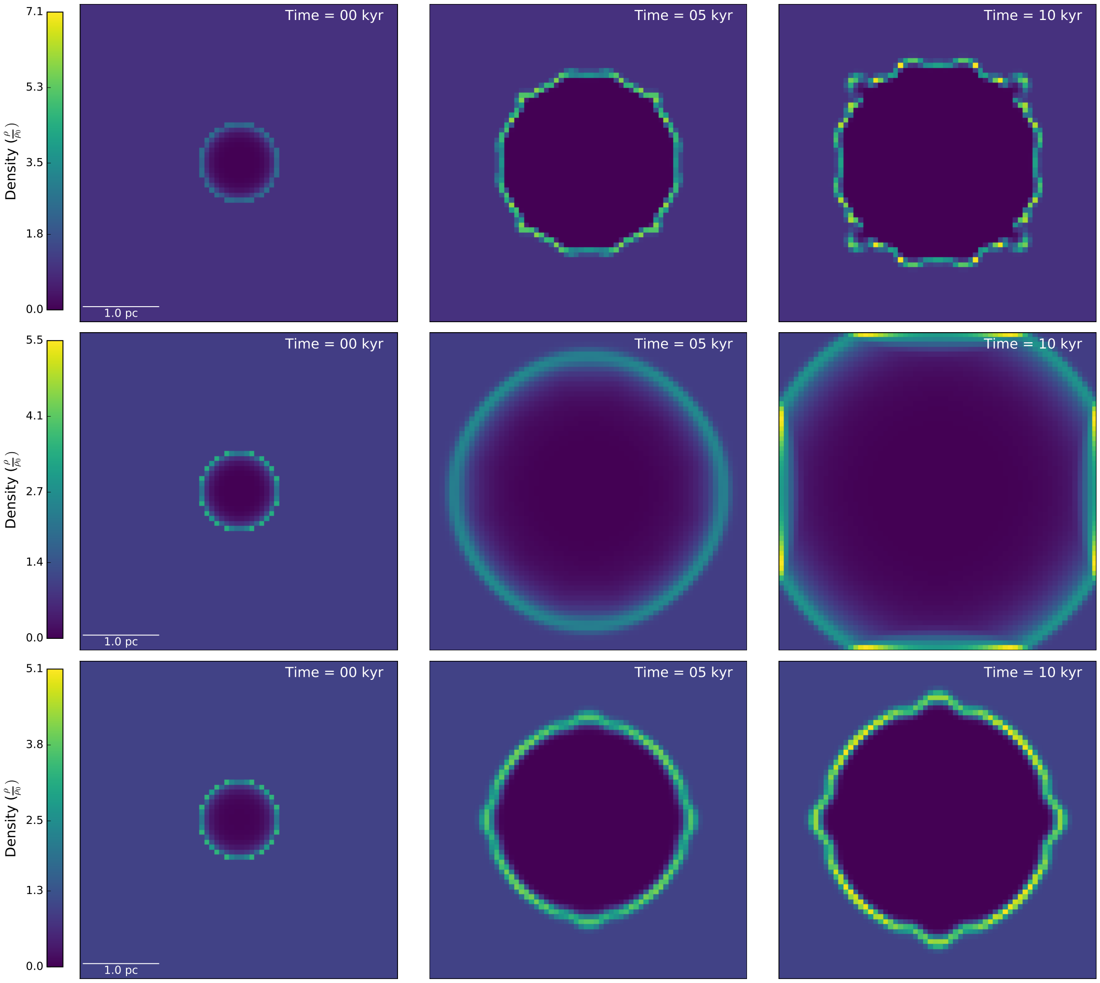

Figure 4.18: A plot comparing the evolution of a supernova blast wave with an initial radius of 8 cells. The top row uses the polytropic equation of state, the middle is the ideal equation of state without cooling, and the bottom row is the ideal equation of state with cooling enabled.

Chapter 5

The Supernova-Driven Box

In this chapter I discuss applying the Supernova module that I have developed in this project to an examination of supernova-driven turbulence. I begin by outlining the motivation for the application, before briefly covering the methods used to generate the conditions within the simulation. I then present a quick analysis of the results, before ending with a discussion of additional simulations that could be run to further this study.

5.1 Motivation for the Supernova-Driven Box

As discussed in §2.2.3 turbulence is thought to play a significant role in the evolution of molecular gas clouds, and to also effect the observed SFR and SFE. Supernovae are known to play a role in the generation of this turbulence, however the scale of this role is yet to be determined. A full simulation of the evolution of a galactic region is beyond the scope of this thesis, so the application that I am presenting in this chapter is an analysis of turbulence generated solely under driving from supernovae.

The simulation begins with a box of uniform density, and then over time supernovae will be generated at random positions throughout the box according to some time distribution that I discuss in §5.2. The turbulence generated by these supernovae can then be quantified and compared to analytical turbulent models, to determine the regime that the turbulence fits into as well as the effectiveness of supernova at generating large-scale turbulence and structure.

5.2 Implementation of Random Supernovae

In order to run this simulation I include an additional mode for the supernova module to use. This mode, which can be activated by setting **sink_supernova_model** to 3, inserts a supernova at a random point within the simulation box with some time distribution.

To achieve this I make the assumption that the time between successive supernova events in a given galaxy follows a Gaussian distribution. The user can set the average time between successive supernovae by using the **sink_supernova_mean_time** parameter, noting that this is given in years. And they can modify standard deviation of the gaussian through **sink_supernova_sigma_time**.

The values that I use for the simulation were based on an estimation of the galactic supernova rate of 20 ± 8 supernovae per millennia [Leibundgut 1998]. Converting this into *time per supernova* yields the average time between supernova events for the whole galaxy. This rate was then scaled down to the size of the simulation box (a 250 pc cube) to yield a final time of 180 ± 72 kyr per supernova event. This is an equivalent distriution to the one used in a recent test of supernova driving in molecular clouds [Padoan et al. 2016].

In order to ensure that the supernovae were inserted at times given by this distribution, whenever the code inserts a supernova it calculates the next insertion time. This is done by using rejection sampling to draw a random point from within 3σ of the average time between events and then adds that delay to the current simulation time. The supernova code will not run again until after the next insertion time.

To ensure replicability of the simulations, I seed the random number generator with **sink_supernova_seed**.

5.3 Simulation Parameters

For this series of simulations I use a cube with a side length of 250 pc and a uniform density of 5 cm^{-3}. The gas is an ideal gas, with an adiabatic constant of $\gamma = \frac{5}{3}$. Supernovae were inserted with a time distribution of 180 ± 72 kyr at random points within the simulation box, and at a fixed initial radius of 8 cells at the simulation resolution. Each supernova has a uniform energy of 10^{51} erg, and deposits 2.5 M$_\odot$ of mass into the box. While this does affect the mass conservation within the box, the injected mass per supernova is around a two-millionth of the total mass within the box, so we can reasonably ignore this violation of the mass conservation. The tests were run with two levels of resolution, 128^3 and 256^3, to examine the turbulent driving on multiple resolution levels.

For these tests gravity was turned off, both to stop the sink particles that would be generated with the supernovae from attracting the gas, but to also to stop the gas itself from self-gravitating. This ensures that any density fluctuations that we measure are a result of the supernova-driven turbulence alone.

Due to time-constraints the simulations were only run for relatively short periods of time: the 256^3 simulation was only able to run for a period of 10 Myr, while the 128^3 simulation was able to run for 40 Myr. As such, the 128^3 simulation will form the basis for the analysis of the supernova-driven turbulence over long time-scales.

5.4 Required Modifications to the Supernova Module

The initial stages of testing for this application revealed a flaw in the momentum conservation method used in the supernova module. If the existing density within a given cell is several orders of magnitude smaller than the ambient density, then the velocity added to the cell is correspondingly several orders of magnitude higher than the solution says it should be.

While this does not immediately seem like an issue, due to the very high speeds that are already within a supernova this can cause unphysical situations very quickly, such as the gas within the cell being superluminal. Additionally, due to the CFL condition (§2.3.5) even if the cell was not breaking the speed of light it would severely impact the maximum allowable time-step, often taking hours of simulation time for the time-step to recover back to normal levels.

To fix this issue I implement a minimum density threshold for inserting the supernova solution. If any cell within the supernova radius had a density below this threshold — set to 10^{-3} cm^{-3} in this experiment — then the region within the radius would be flattened to the ambient density before inserting the solution. Otherwise, the solution would be inserted as standard. This completely solves the issue in the remainder of the simulations.

5.5 Projections of the Simulation

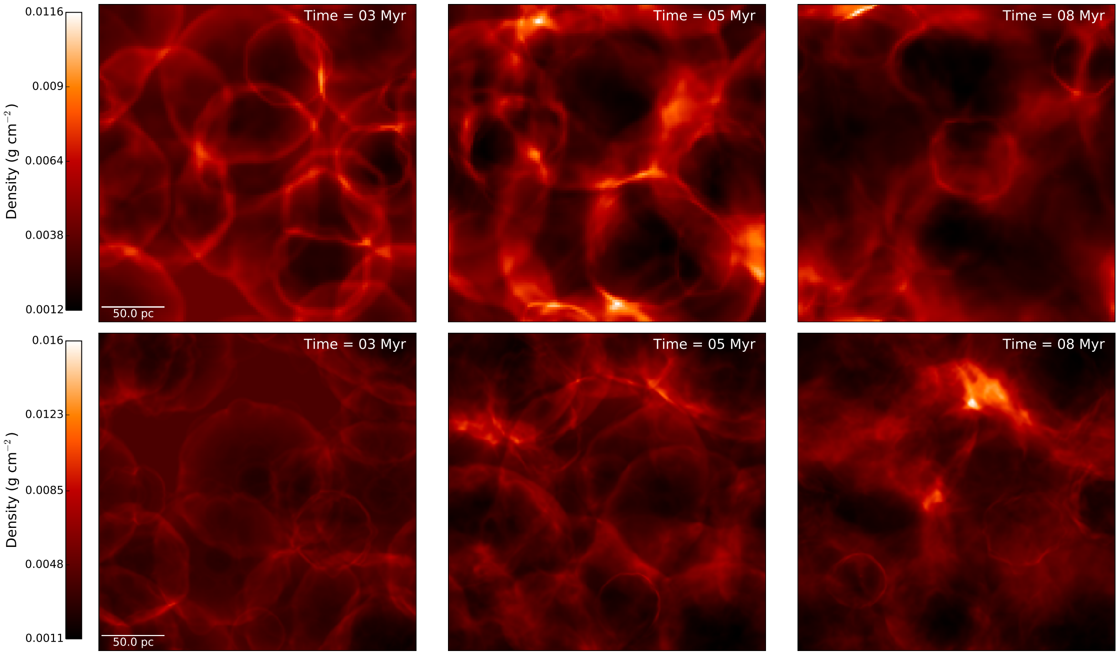

Figure 5.1: Plots of column density projections along the z-axis of the simulation box. The top row is at a resolution of 128^3 cells, and the bottom row is at 256^3 cells. The mean column density in the box is 4×10^{-3} g cm^{-2}.

One interesting feature to examine after the simulations finished is the projected density along one axis of the simulation box. Figure 5.1 shows a comparison of the projected densities between the two resolutions that I ran over the simulation time of the 256^3 as it is the shorter simulation. Comparing the two shows that during the initial 3 Myr the simulation boundaries were full of discrete supernova events. The boundaries of the supernovae are clear, and there are visible sections of disturbed gas in the projection. Moving to the 5 Myr projection we observe that there are less discrete supernovae visible as the gas within the box becomes more uniformly driven. Finally in the 8 Myr projections we can see typical turbulent ISM structure beginning to appear.

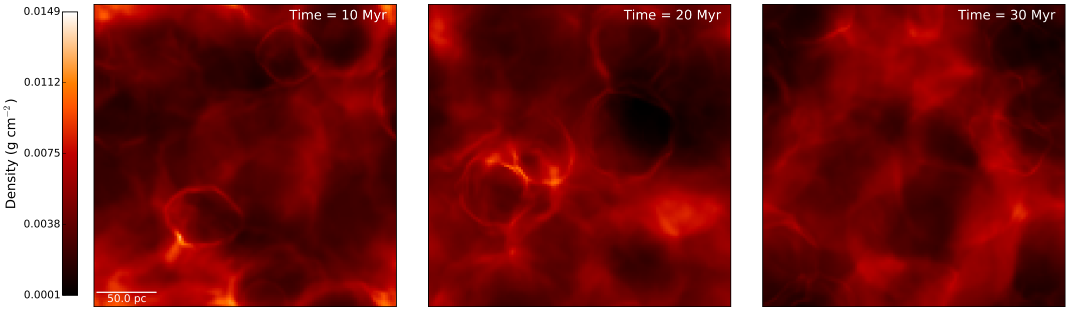

Figure 5.2: Plots of column density projections along the z-axis of the simulation box. The resolution of the simulation is 128^3 cells. The mean column density in the box is 4×10^{-3} g cm^{-2}.

Figure 5.2 shows the projected density along the z axis of the box within the 128^3 resolution test. This is over a far longer time-scale than Figure 5.1. In this set of images we can see homogeny appearing in the structure of the projected gas density.

5.6 Analysis

In this section I will present my analysis of the supernova driven box in two key parts, each focussing on a different method that is typically used in turbulence analysis for simulations. The first is the *Probability Density Function* (PDF), which encodes the distribution of a particular variable over the whole range of values. PDFs allow for an easy visualising of the concentrations and overall structure of a given variable. My use of PDFs will focus on three key quantities within the box: the density, the temperature, and the velocity.

The second tool is the *Power Spectrum*, this is a Fourier transform of a measurable quantity within the box, such as the density or the velocity. It can be used to describe the spatial distribution — and the contrasts therein — of the quantity being analysed throughout the simulation region. The power spectra allow us to make classify the nature of the turbulence, relating it to models of turbulence and past comparisons of the types of turbulence [Frisch 1995].

5.6.1 Examining the Distributions

Before starting the analysis it is worth noting that due to the scales at which the density fluctuations with a given region act, it is often difficult to present a density PDF on a linear scale. Additionally, past studies of the density fluctuations in an isothermal gas is log-normal [Vazquez-Semadeni 1994]. As such the convention for analysing the density PDF requires the definition of a new variable s, as follows.

Define a new parameter $s = \ln \frac{\rho}{\langle\rho\rangle}$, where $\langle\rho\rangle$ is the expected value of the density within the simulation box, i.e. the mean density. Note that this new parameter is dimensionless, by creating it we have effectively removed the dimensionality of the problem. This ties in with the fundamental benefit of the density PDF in this form, by normalising the density first by the mean density, we have removed the dependence the results have on the simulation parameters. This means that it is much easier to directly compare the results of two simulations, or to examine problems with entirely different scales.

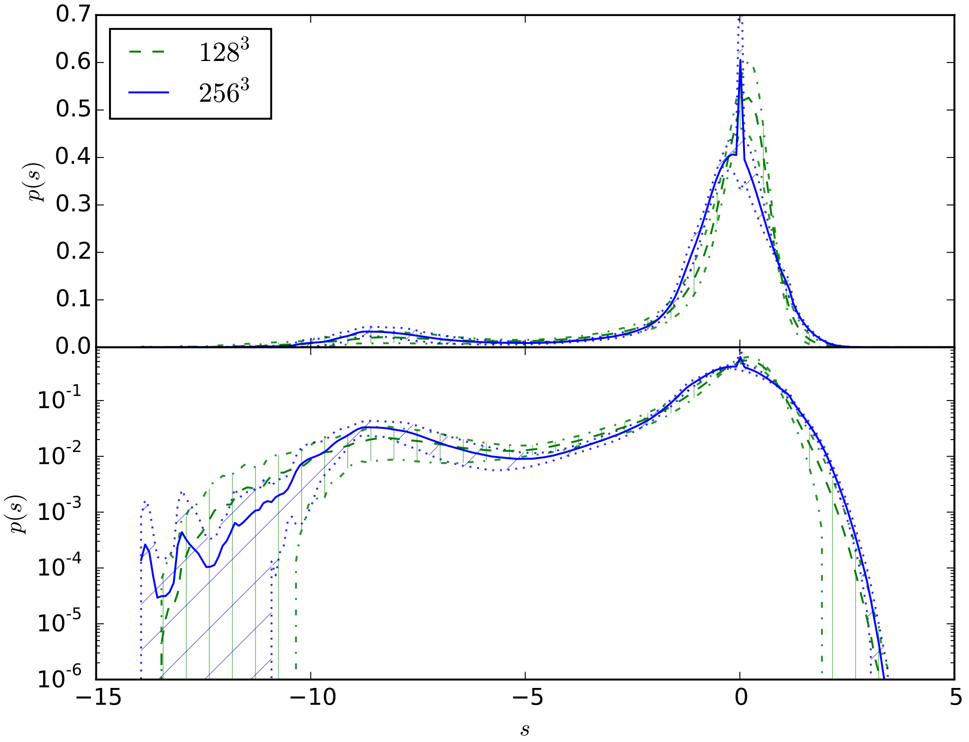

Figure 5.3: A plot of the density PDF for the two different resolutions used in the simulation. The PDF has been averaged from the density PDF over the course of the simulation, with one standard deviation either side by the dotted lines and faint hatching.

From preliminary examinations I determined that the simulation took around around 5 Myr to reach an equilibrium with the energy inserted vs energy lost. This is due to the fact that the box was originally entirely at rest with a uniform density so it takes a while for a stable supernova-driven state to appear within the box. All data analysis from this point will be done using a time-averaged set of data, that begins 5 Myr into the simulation. The time-averaging is done by first calculating the PDF for each set of data produced by the simulation, and then averaging the PDFs. I also produce a standard deviation of the value at each point within the PDF. This is shown on the plots as a two neighbouring dotted lines of the same color as the main PDF.

Figure 5.3 depicts the density PDF within the box for the two resolution levels examined. While there is a clear central Gaussian or skewed distribution that contains the majority of the gas in both simulations, there is the presence of long extended tail to the left of this peak. This implies the presence of significantly less dense regions within the simulation.

It is worth noting that simulations of this kind are usually done using isothermal gas, whereas this test uses an ideal gas. The manifestation of this difference is that the density PDF of an isothermal gas is a log-normal distribution [Vazquez-Semadeni 1994; Passot and Vázquez-Semadeni 1998] as the gas has a single phase. However, in the simulations that I am running the gas has two phases as a result of the cooling function, there is very hot gas (~ 10^8 K) that occurs immediately following a supernova event, and warm gas (~ 10^4 K) that cannot be cooled as the cooling curve data does not extend below this limit [Sutherland and Dopita 1993]. The presence of these two phases causes the tail that we see in the density PDF.

This leads directly into the examination of the temperature PDF for the simulation box, which can be found in Figure 5.4. The PDF shows fairly consistent temperature distributions within the simulation box across both resolutions, with the presence of three main temperature peaks. The peaks in the temperature PDF correspond to the following (from left to right):

- Gas that has been minimally affected by the supernova explosions, and heated by compression (10 – 100 K),
- Gas that has cooled after being in a supernova, or has been compressed significantly (100 – 10^6 K),
- Gas that was recently in a supernova explosion (10^6 +).

We can also take advantage of the different lengths of time that the simulations ran for, to examine the evolution of the average temperature distribution within the box. The 128^3 line shows a significant peak at a temperature of 10^4 K. This is the minimum temperature at which the used Sutherland-Dopita cooling curve has data, so it is also the minimum temperature that the cooling module will cool to. As such, the gas within the simulation will tend towards 10^4 K as the simulation progresses.

One relationship that is worth exploring from the simulations is the density-temperature relationship. Figure 5.5 shows the number of cells with a density ρ and a temperature T for different times throughout the 128^3 cell test. It is worth noting that the majority of the cells in the simulation are slightly above the mean density (5.185×10^{-24} g cm^{-3}) and with a temperature between 10^2 and 10^4 K. We can also see that the majority of

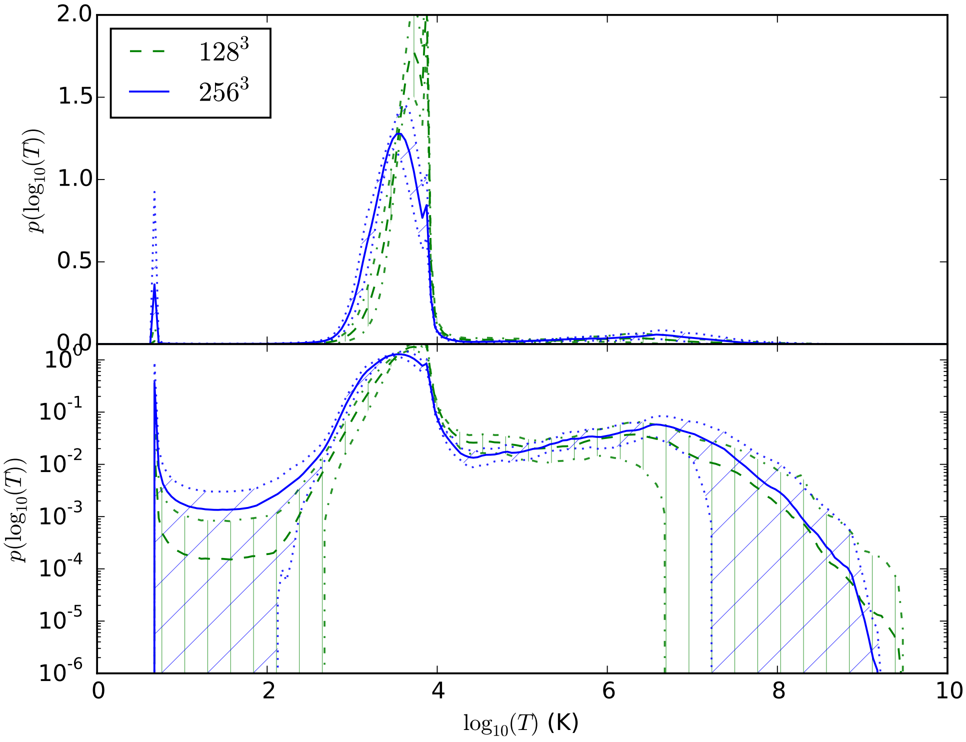

Figure 5.4: A plot of the PDF for $\log_{10}(T)$ for the two different resolutions examined in this experiment. The PDF has averaged from the $\log_{10}(T)$ PDF calculated at different times throughout the simulation, with one standard deviation also provided.

the gas that is above the 10^4 K threshold for cooling is at least an order of magnitude below the mean density.

An interesting feature is the line at the top of the middle image in Figure 5.5. That plot occurs immediately after the insertion of a supernova, so the line is a supernova. The fact that we have a direct representation of a supernova in these images allows us to infer a great deal about how the supernovae drive the relationship between density and temperature. The supernova covers two orders of magnitude in both temperature and density, however the minimum temperature inserted is still an order of magnitude higher than the next highest temperature in the box.

Finally, we wish to examine the Mach number distribution throughout the box. The Mach number, henceforth denoted as $\mathcal{M}$, is the ratio of the velocity to the speed of sound within the gas. For the purposes of the PDF I calculated the local value of $\mathcal{M}$ by determining the local velocity within the cell, and then determining the speed of sound in an ideal gas using:

$$c_s = \sqrt{\frac{\gamma k_B T}{\mu m_H}}, \tag{5.1}$$

for $\gamma = \frac{5}{3}$, and $\mu = 1$ for typical values for the interstellar medium.

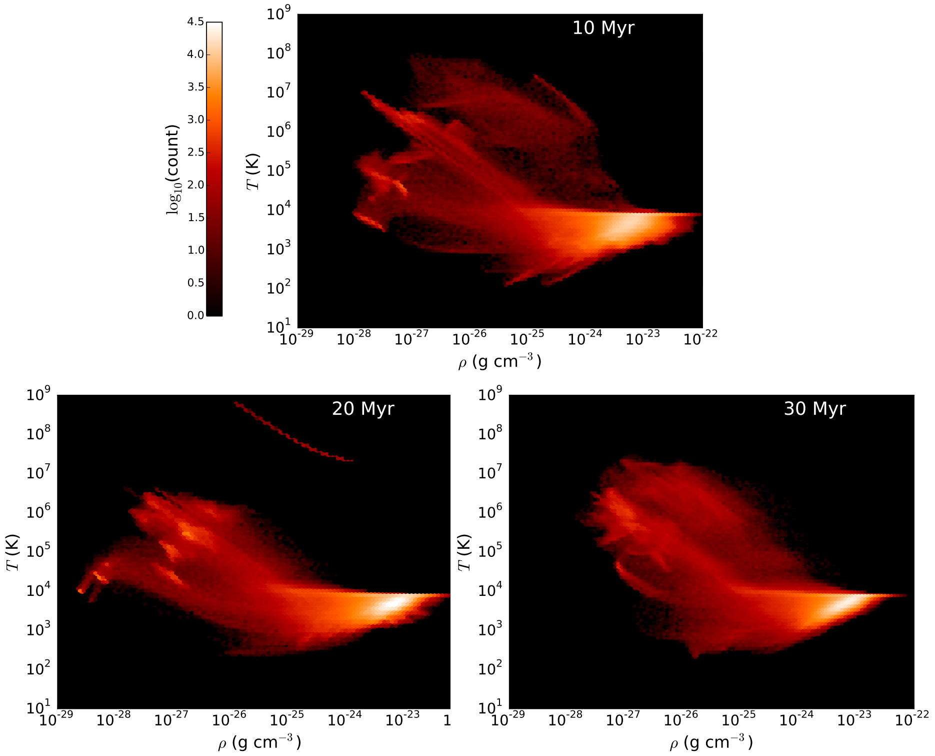

Figure 5.5: A set of heat maps showing the distribution of the temperature and the gas for the 128^3 test. The mean density within the box is 5.185×10^{-24} g cm^{-3}. One feature to examine is the line at the top of the lower left image, this is a supernova that has just exploded. In order of the time since the last supernova explosion the plots are: lower left, top, lower right, which provides an indication of the way that gas responds to a supernova.

The PDF for $\mathcal{M}$ can be seen in Figure 5.6. It shows that a significant portion of the gas in the box is transonic.

5.6.2 Examining the Power Spectra

There are two power spectra that I will be calculating in this analysis, the density power spectrum, $P(k)$, and the velocity power spectrum, $E(k)$. The density power spectrum is the 3D Fourier transform of the density within the box, given by

$$P(k)\,dk = 4\pi \int \langle \hat{\rho}\hat{\rho}^{\star} \rangle\, k^2\, dk. \tag{5.2}$$

The velocity power spectrum is defined in the same way,

$$E(k)\,dk = 4\pi \int \langle \hat{v}\hat{v}^{\star} \rangle\, k^2\, dk, \tag{5.3}$$

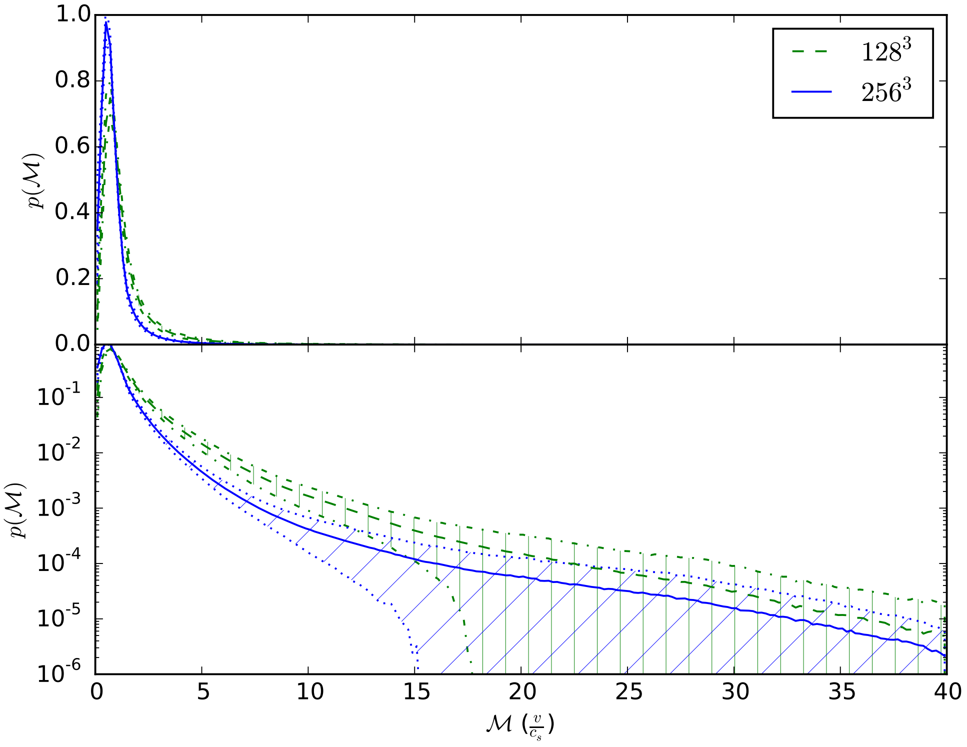

Figure 5.6: A plot of the PDF of the Mach number within the simulation for the two different resolution levels examined in this experiment. The PDF was calculated and then averaged for the whole simulation length, with one standard deviation provided.

where in both cases $\hat{x}$ denotes the Fourier transform of x, and $x^\star$ denotes the complex conjugate of x.

The calculated time-averaged density and velocity power spectra for the simulations can be found in Figure 5.7. In this figure I have assumed an *inertial range* of $5 \leq k \leq 15$ based on estimates of the inertial range I have seen in previous work [Kritsuk et al. 2007; Schmidt et al. 2009; Federrath et al. 2009]. However, it should be noted that all of those simulations used far higher resolutions than the simulations that I am analysing (2048^3, 768^3, and 1024^3 respectively), and typically resolutions of at least 512^3 are required to accurately measure the k dependence of the power spectra in the inertial region[Kritsuk et al. 2007; Federrath et al. 2010].

Resolution	a	b
128^3	-1.67	-2.19
256^3	-1.65	-1.36

Table 5.1: A table showing the power law exponents a and b of the density power spectrum, $P(k) \propto k^a$, and the velocity power spectrum, $E(k) \propto k^b$, within the inertial range shown in Figure 5.7.

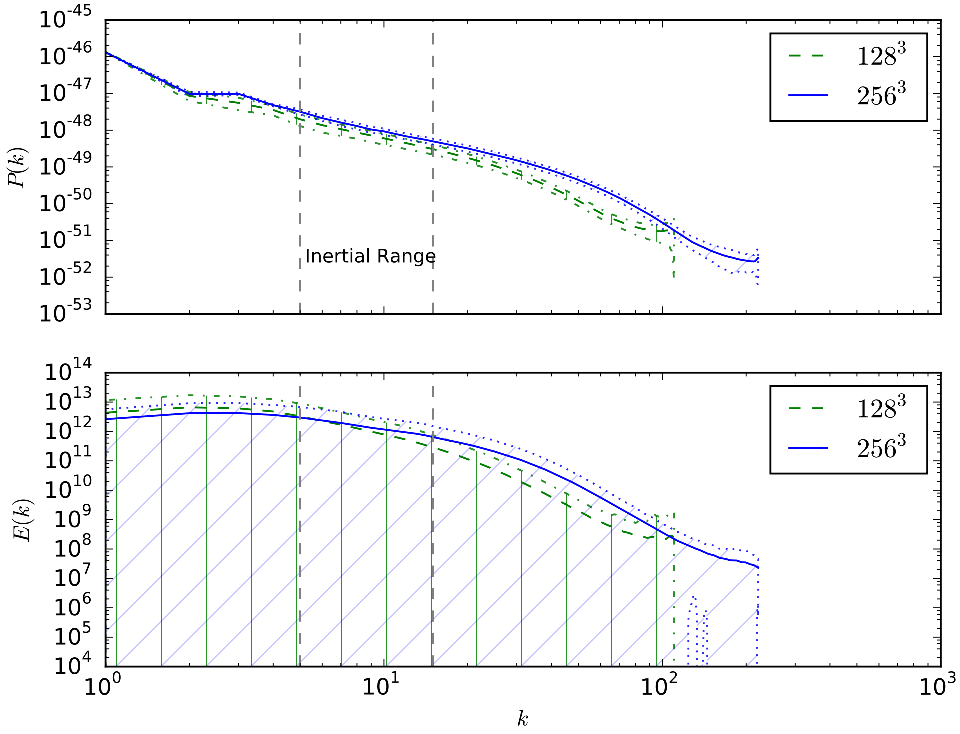

Figure 5.7: The density and velocity power spectrum for the simulations.

With this in mind, I calculated the power law for each of the spectra shown in Figure 5.7 by using a linear fit to the data seen in the figure — i.e. $\log_{10} P(k)$ against $\log_{10} k$ — within the inertial range. This produced the values found in Table 5.1. The $P(k)$ proportionality is consistent between the two resolutions. The power law values are close, and Figure 5.7 shows small standard deviations from the mean for $P(k)$.

Conversely, the $E(k)$ proportionality fluctuates between the two resolution levels, and as can be seen by the large standard deviations in Figure 5.7 the variance of $E(k)$ over time within the same simulation is also large. This is a result of the discrete driving events caused by the supernovae, compared to a constant driving force that would be used in typical simulations to measure turbulence.

As the $E(k)$ values are calculated based on the average values of the velocity spectra from the entire simulation we can assume that the 128^3 proportionality woud be closer to the actual value from supernova-driven turbulence as it is the average of 6 times more individual spectra. This yields a value of $E(k) \propto k^{-2.19}$. This is closer to the Burgers model of turbulence, which has a power of k^{-2} [Burgers 1948] than the Kolmogorov model of $k^{-\frac{5}{3}}$ [Kolmogorov 1941; Kolmogorov 1962]. This is a reasonable result as the Burgers model deals with compressive turbulence and supernovae are source of compressive turbulence.

The result of $P(k) \propto k^{-1.67}$ is also reasonable, it is close to the value achieved in [Federrath et al. 2009] of $k^{-1.44}$. The discrepancy in this case would be due to the magnitude of the driving Mach number — $\mathcal{M}$~5.5 in their case compared to $\mathcal{M}$~1 in my simulations — noting that the exponent in the $P(k)$ power law scales down with increasing $\mathcal{M}$ [Kim and Ryu 2005]. My value is also close to the power law relationship for a weakly compressible isothermal flow at transonic $\mathcal{M}$ of $k^{-1.7}$ [Kritsuk et al. 2007]. However, in both of these cases the simulations were run using a isothermal gas, compared to the ideal gas in these simulations.

5.7 Future Work

The main area I would like to expand this experiment would be to increase both the resolution levels being used, and the simulation time. This would improve the validity of the power spectrum analysis, and provide a more comprehensive look at the relationship between the supernova heating and the limitations of the cooling range. The original outline for this experiment did contain a simulation at a resolution of 512^3, however due to time constraints and unforeseen complications this was not feasible for inclusion in this thesis.

Beyond this, I would like to use this module, along with the Sink Particle, and jet-outflow models already in FLASH4 [Federrath et al. 2010; Federrath et al. 2014]to examine the effect of the introduced supernova turbulence on the SFR and SFE, extending the application presented in [Federrath et al. 2014]. This was originally one of the stretch goals for this project, and it would be good to see it completed.

In terms of the model itself, the method of momentum insertion is currently unstable for large density fluctuations within the supernova radius as I found during the initial stages of this experiment. This can be avoided by inserting the Sedov profiles directly rather than attempting to maintain the existing gas structure. However, I would like to find a better method for doing this, such as inserting the profiles over some time spread to avoid sudden large changes in the velocity within cells.

Finally, I would like to include a more recent version of the Sutherland-Dopita cooling function. The version that is currently being used is the original table from 1993. I am aware that more recent tables present cooling function values for a wider range of temperatures, and the cut-off of 10^4 K did present a significant impact on the results of the supernova-driven turbulence.

Chapter 6

Conclusion

In this thesis I have presented a realistic sub-grid implementation of supernovae in the FLASH4 framework. This work required significant background knowledge that I outlined in Chapters 1 and 2, as well as relying heavily on the analytical Sedov solution. I presented a complete derivation of this solution in Chapter 3, and extended the model to include a specific internal energy profile, and estimates of the life-time of the Sedov phase of supernova evolution.

I presented the development process of supernova implementation, in which we found that the supernova's internal energy is necessary to ensure spherical evolution of the produced supernova blast wave, whereas pure kinetic energy models such as using an isothermal hydrodynamics solver exhibit significant instabilities in their blast waves. The final implementation was found to evolve identically to the analytical Sedov solution, a widely used benchmark for checking the validity of supernova implementations.

Finally, I used the supernova implementation to examine the effects of supernova-driven turbulence in the interstellar medium. I simulated a 250 pc cube of gas at resolutions of 128^3 and 256^3 cells, in which I introduced supernovae at random positions at an equivalent rate to the estimated galactic supernova rate. I found that the density PDF produced by the supernova-driven turbulence is constant throughout the simulation period, with a formation period of around 5 Myr. The density PDF showed a two phase medium that was a product of the high temperatures introduced locally in a supernova, and the warm background resulting from the lower bound on cooling function used.

I calculated the density power spectrum for the each of the tests and found strong correlation between the two levels, and a very small amount of time variance. The density spectral law was calculated to be $P(k) \propto k^{-1.67}$, very close to the estimated value for weakly compressive transonic turbulence in an isothermal gas of $k^{-1.7}$. I found that the velocity power spectrum varied significantly over time, a result from the fact that the supernovae provide discrete driving events rather than continuous driving. The average velocity spectral law was calculated for the longest running simulation and deteremined to be $E(k) \propto k^{-2.19}$. This is in line with the Burgers model for compressive turbulence.

Finally, I outlined plans for the continuing development of the supernova implementation, and the study of supernova driven turbulence; namely getting an updated version of the cooling curve that covers a wider range of temperatures, and running a 512^3 resolution simulation of the supernova driving. I also presented a long-term goal to use the supernova implementation to examine the effect of the supernova-driven turbulence on the SFR and SFE within galactic clouds. This would be an extension of the work presented in [Federrath et al. 2014].

Bibliography

Bate, M. R., Bonnell, I. A., and Price, N. M. 1995. Modelling accretion in protobinary systems. *277*, 362–376. (p. 26)

Bouchut, F., Klingenberg, C., and Waagan, K. 2010. A multiwave approximate riemann solver for ideal mhd based on relaxation ii: numerical implementation with 3 and 5 waves. *Numerische Mathematik 115*, 4, 647–679. (p. 11)

Bregman, J. N. 1980. The galactic fountain of high-velocity clouds. *236*, 577–591. (p. 3)

Bubel, A.-P. 2016. A supernova feedback implementation for the astrophysical simulation software Arepo. *ArXiv e-prints*. (p. 30)

Burgers, J. M. 1948. A mathematical model illustrating the theory of turbulence. *Advances in applied mechanics 1*, 171–199. (p. 64)

Cappellaro, E., Evans, R., and Turatto, M. 1999. A new determination of supernova rates and a comparison with indicators for galactic star formation. *arXiv preprint astro-ph/9904225*. (p. 5)

Chandrasekhar, S. 1935. The highly collapsed configurations of a stellar mass (second paper). *Monthly Notices of the Royal Astronomical Society 95*, 207–225. (pp. 5, 28)

Choptuik, M. W. 1993. Universality and scaling in gravitational collapse of a massless scalar field. *Physical Review Letters 70*, 1, 9. (p. 1)

Courant, R., Friedrichs, K., and Lewy, H. 1967. On the partial difference equations of mathematical physics. *IBM journal 11*, 2, 215–234. (p. 12)

Dong, S., Shappee, B. J., Prieto, J. L., Jha, S. W., Stanek, K. Z., Holoien, T. W.-S., Kochanek, C. S., Thompson, T. A., Morrell, N., Thompson, I. B., Basu, U., Beacom, J. F., Bersier, D., Brimacombe, J., Brown, J. S., Bufano, F., Chen, P., Conseil, E., Danilet, A. B., Falco, E., Grupe, D., Kiyota, S., Masi, G., Nicholls, B., Olivares E., F., Pignata, G., Pojmanski, G., Simonian, G. V., Szczygiel, D. M., and Woźniak, P. R. 2016. Asassn-15lh: A highly super-luminous supernova. *Science 351*, 6270, 257–260. (p. 3)

Dubois, Y. and Teyssier, R. 2008. Supernova Feedback in Galaxy Formation. In J. H. Knapen, T. J. Mahoney, and A. Vazdekis Eds., *Pathways Through an Eclectic Universe*, Volume 390 of *Astronomical Society of the Pacific Conference Series* (June 2008), pp. 388. (p. 25)

Eddington, A. S. 1924. On the relation between the masses and luminosities of the stars. *84*, 308–332. (p. 5)

Elmegreen, B. G. and Scalo, J. 2004. Interstellar turbulence i: observations and processes. *arXiv preprint astro-ph/0404451*.

Estalella, R. 2013. Jets and outflows. (p. 4)

Federrath, C., Banerjee, R., Clark, P. C., and Klessen, R. S. 2010. Modeling Collapse and Accretion in Turbulent Gas Clouds: Implementation and Comparison of Sink Particles in AMR and SPH. *713*, 269–290. (pp. 26, 65)

Federrath, C. and Klessen, R. S. 2012. The Star Formation Rate of Turbulent Magnetized Clouds: Comparing Theory, Simulations, and Observations. *761*, 156. (pp. 1, 9)

Federrath, C., Klessen, R. S., and Schmidt, W. 2008. The Density Probability Distribution in Compressible Isothermal Turbulence: Solenoidal versus Compressive Forcing. *688*, L79. (pp. 8, 10)

Federrath, C., Klessen, R. S., and Schmidt, W. 2009. The Fractal Density Structure in Supersonic Isothermal Turbulence: Solenoidal Versus Compressive Energy Injection. *692*, 364–374. (p. 64)

Federrath, C., Rathborne, J. M., Longmore, S. N., Kruijssen, J. M. D., Bally, J., Contreras, Y., Crocker, R. M., Garay, G., Jackson, J. M., Testi, L., and Walsh, A. J. 2016. The link between solenoidal turbulence and slow star formation in G0.253+0.016. *ArXiv e-prints*. (p. 9)

Federrath, C., Schrön, M., Banerjee, R., and Klessen, R. S. 2014. Modeling Jet and Outflow Feedback during Star Cluster Formation. *790*, 128. (pp. 1, 2, 4, 10, 65, 68)

Frisch, U. 1995. *Turbulence: the legacy of AN Kolmogorov*. Cambridge university press. (pp. 8, 58)

Fryxell, B., Olson, K., Ricker, P., Timmes, F. X., Zingale, M., Lamb, D. Q., MacNeice, P., Rosner, R., Truran, J. W., and Tufo, H. 2000. FLASH: An Adaptive Mesh Hydrodynamics Code for Modeling Astrophysical Thermonuclear Flashes. *131*, 273–334. (pp. 1, 10)

Gallagher, B. 2012. Gas hydrodynamics. (p. 11)

Getman, K. V., Feigelson, E. D., Luhman, K. L., Sicilia-Aguilar, A., Wang, J., and Garmire, G. P. 2009. Protoplanetary disk evolution around the triggered star-forming region cepheus b. *The Astrophysical Journal 699*, 2, 1454. (p. 4)

Green, D. A. 2002. Historical supernovae and their remnants. *Highlights of Astronomy 12*, 350–353. (p. 3)

Hennebelle, P. and Chabrier, G. 2011. Analytical star formation rate from gravoturbulent fragmentation. *The Astrophysical Journal Letters 743*, 2, L29.

Hennebelle, P. and Falgarone, E. 2012. Turbulent molecular clouds. *The Astronomy and Astrophysics Review 20*, 1, 1–58.

Hillebrandt, W., Nomoto, K., and Wolff, R. G. 1984. Supernova explosions of massive stars - The mass range 8 to 10 solar masses. *133*, 175–184. (pp. 6, 28)

Hockney, R. W. and Eastwood, J. W. 1988. *Computer simulation using particles*. (p. 11)

Hoefner, S. 2010. Dynamical evolution of supernova remnants. [Online; accessed 2016-03-10]. (p. 30)

Hugoniot, H. 1887. Memoir on the propagation of movements in bodies, especially perfect gases (first part). *J. de l'Ecole Polytechnique 57*, 3–97.

Jeans, J. H. 1902. The stability of a spherical nebula. *Philosophical Transactions of the Royal Society of London. Series A, Containing Papers of a Mathematical or Physical Character 199*, 1–53. (p. 4)

Kainulainen, J., Federrath, C., and Henning, T. 2013. Connection between dense gas mass fraction, turbulence driving, and star formation efficiency of molecular clouds. *Astronomy & Astrophysics 553*, L8. (p. 10)

Khokhlov, A., Mueller, E., and Hoeflich, P. 1993. Light curves of Type IA supernova models with different explosion mechanisms. *270*, 223–248. (p. 6)

Kim, J. and Ryu, D. 2005. Density power spectrum of compressible hydrodynamic turbulent flows. *The Astrophysical Journal Letters 630*, 1, L45. (p. 65)

Klessen, R. S. and Hennebelle, P. 2010. Accretion-driven turbulence as universal process: galaxies, molecular clouds, and protostellar disks. *Astronomy & Astrophysics 520*, A17. (p. 9)

Kolmogorov, A. N. 1941. The local structure of turbulence in incompressible viscous fluid for very large reynolds numbers. In *Dokl. Akad. Nauk SSSR*, Volume 30 (1941), pp. 301–305. JSTOR. (p. 64)

Kolmogorov, A. N. 1962. A refinement of previous hypotheses concerning the local structure of turbulence in a viscous incompressible fluid at high reynolds number. *Journal of Fluid Mechanics 13*, 01, 82–85.

Kritsuk, A. G., Norman, M. L., Padoan, P., and Wagner, R. 2007. The statistics of supersonic isothermal turbulence. *The Astrophysical Journal 665*, 1, 416. (pp. 63, 65)

Krumholz, M. R. and McKee, C. F. 2005. A general theory of turbulence-regulated star formation, from spirals to ultraluminous infrared galaxies. *The Astrophysical Journal 630*, 1, 250.

Krumholz, M. R., McKee, C. F., and Klein, R. I. 2006. Bondi-hoyle accretion in a turbulent medium. *The Astrophysical Journal 638*, 1, 369. (p. 9)

Krumholz, M. R., McKee, C. F., and Tumlinson, J. 2009. The star formation law in atomic and molecular gas. *The Astrophysical Journal 699*, 1, 850. (p. 9)

Lada, C. J. and Lada, E. A. 2003. Embedded Clusters in Molecular Clouds. *41*, 57–115. (p. 26)

Larson, R. B. 1981. Turbulence and star formation in molecular clouds. *Monthly Notices of the Royal Astronomical Society 194*, 4, 809–826. (p. 10)

Leibundgut, B. 1998. Supernova rates. *Neutrino Astrophysics*, 51. (p. 56)

Mac Low, M.-M., Balsara, D. S., Kim, J., and de Avillez, M. A. 2005. The distribution of pressures in a supernova-driven interstellar medium. i. magnetized medium. *The Astrophysical Journal 626*, 2, 864. (p. 3)

Mac Low, M.-M. and Klessen, R. S. 2004. Control of star formation by supersonic turbulence. *Reviews of Modern Physics 76*, 125–194. (pp. 1, 9)

Mannucci, F., Maoz, D., Sharon, K., Botticella, M., Della Valle, M., Gal-Yam, A., and Panagia, N. 2008. The supernova rate in local galaxy clusters. *Monthly Notices of the Royal Astronomical Society 383*, 3, 1121–1130.

McKee, C. F. 1989. Photoionization-regulated star formation and the structure of molecular clouds. *345*, 782–801. (p. 9)

McKee, C. F. and Ostriker, E. C. 2007. Theory of star formation. *arXiv preprint arXiv:0707.3514*.

Mushotzky, R. 2010. Super nova and super nova remnants. [Online; accessed 2016-10-26]. (p. 30)

Noether, E. 1918. Invariante variationsprobleme, nachr. d. könig. gesellsch. d. wiss. zu göttingen, math-phys. klasse (1918) 235–257. *English Reprint: physics/0503066, http://dx.doi.org/10.1080/00411457108231446*, 57. (p. 11)

Padoan, P., Federrath, C., Chabrier, G., Evans, N. J., II, Johnstone, D., Jørgensen, J. K., McKee, C. F., and Nordlund, Å. 2014. The Star Formation Rate of Molecular Clouds. *Protostars and Planets VI*, 77–100.

Padoan, P., Juvela, M., Pan, L., Haugbølle, T., and Nordlund, Å. 2016. Supernova Driving. III. Synthetic Molecular Cloud Observations. *826*, 140. (p. 56)

Passot, T. and Vázquez-Semadeni, E. 1998. Density probability distribution in one-dimensional polytropic gas dynamics. *Physical Review E 58*, 4, 4501.

Peleg, Y., Bose, S., and Parker, L. 1997. Choptuik scaling and quantum effects in 2d dilaton gravity. *Physical Review D 55*, 8, R4525. (p. 1)

Piontek, R. A. and Ostriker, E. C. 2004. Thermal and magnetorotational instability in the interstellar medium: Two-dimensional numerical simulations. *The Astrophysical Journal 601*, 2, 905. (p. 9)

Piontek, R. A. and Ostriker, E. C. 2007. Models of vertically stratified two-phase ism disks with mri-driven turbulence. *The Astrophysical Journal 663*, 1, 183.

Rankine, W. M. 1870. On the thermodynamic theory of waves of finite longitudinal disturbance. *Philosophical Transactions of the Royal Society of London*, 277–288. (p. 15)

Reynolds, O. 1883. An experimental investigation of the circumstances which determine whether the motion of water shall be direct or sinuous, and of the law of resistance in parallel channels. *Proceedings of the royal society of London 35*, 224-226, 84–99.

Ryden, B. 2011. Spherical blastwaves and supernova remnants. [Online; accessed 2016-02-25]. (p. 21)

Salim, D. M., Federrath, C., and Kewley, L. J. 2015. A universal, turbulence-regulated star formation law: From milky way clouds to high-redshift disk and starburst galaxies. *The Astrophysical Journal Letters 806*, 2, L36.

Schmidt, W., Federrath, C., Hupp, M., Kern, S., and Niemeyer, J. C. 2009. Numerical simulations of compressively driven interstellar turbulence-i. isothermal gas. *Astronomy & Astrophysics 494*, 1, 127–145. (p. 63)

Sedov, L. I. 1959. *Similarity and Dimensional Methods in Mechanics*. (pp. 1, 13)

Simpson, C. M., Bryan, G. L., Hummels, C., and Ostriker, J. P. 2015. Kinetic Energy from Supernova Feedback in High-resolution Galaxy Simulations. *809*, 69. (pp. 30, 31)

Stahler, S. W. and Palla, F. 2008. *Young Stellar Systems*, pp. 88–133. Wiley-VCH Verlag GmbH. (p. 5)

Stokes, G. G. 1851. *On the effect of the internal friction of fluids on the motion of pendulums*, Volume 9. Pitt Press. (p. 8)

Sutherland, R. S. and Dopita, M. A. 1993. Cooling functions for low-density astrophysical plasmas. *88*, 253–327. (pp. 23, 51, 60)

Tammann, G. et al. 1982. Supernovae: A survey of current research. *NATO ASIC Proc. 90), ed. MJ Rees & R.-J. Stoneham (Dordrecht: Reidel) 371*. (p. 6)

Vazquez-Semadeni, E. 1994. Hierarchical Structure in Nearly Pressureless Flows as a Consequence of Self-similar Statistics. *423*, 681. (pp. 59, 60)

Waagan, K., Federrath, C., and Klingenberg, C. 2011. A robust numerical scheme for highly compressible magnetohydrodynamics: Nonlinear stability, implementation and tests. *Journal of Computational Physics 230*, 9, 3331–3351.

Weidemann, V. and Koester, D. 1983. The upper mass limit for white dwarf progenitors and the initial-final mass relation for low and intermediate mass stars. *121*, 77–84. (pp. 5, 28)